ASCE

Liquefaction Susceptibility of Saturated Coral Sand Subjected to Various Patterns of Principal Stress Rotation

Guoxing Chen[1]; Weijia Ma[2]; You Qin[3]; Kai Zhao[4]; and Jun Yang, F.ASCE[5]

Abstract: The influences of consolidation conditions and rotation patterns of principal stress on the liquefaction susceptibility of saturated coral sand have emerged as an interesting problem in recent years. This paper presents results from a comprehensive experimental study comprising undrained monotonic shear tests and undrained cyclic shear tests subjected to various patterns of principal stress rotation. A remarkable finding is that a virtually unique correlation exists between a generalized shear strain amplitude γ_{ga} and the excess pore water pressure ratio r_u irrespective of consolidation conditions and cyclic loading patterns. A simple formulation is then proposed to relate γ_{ga} and r_u. Another significant finding is that the liquefaction susceptibility of coral sand and the correlation between the conventional cyclic stress ratio (CSR) and the number of cycles to failure N_f (corresponding to $\gamma_{ga} = 2.5\%$) are strongly affected by the couplings of consolidation conditions and cyclic loading patterns. By introducing a generalized unit cyclic stress ratio (USR_g) as a new proxy for liquefaction resistance, a strong correlation is found between USR_g and N_f for all data sets from the experiments. An explicit relationship is then proposed for practical application. The wide applicability of this relationship is well demonstrated using the literature data for various undrained cyclic laboratory tests and different sands. **DOI: 10.1061/(ASCE)GT.1943-5606.0002590.** © *2021 American Society of Civil Engineers.*

Author keywords: Saturated coral sand; Liquefaction; Undrained shear behavior; Undrained cyclic shear test; Consolidation condition; Principal stress rotation.

Introduction

Carbonate sand with calcium carbonate ($CaCO_3$) content greater than 90% is often called coral sand. Coral sands exist widely in the tropical and subtropical regions (Burke et al. 2011). The field evidence of coral sand liquefaction has been repeatedly observed during strong earthquakes, e.g., the 1993 M_w 7.7 Guam earthquake (Vahdani et al. 1994), the 2006 M_w 6.7 and M_w 6.0 Hawaii earthquakes (Chock et al. 2006), and the 2010 M_w 7.0 Haiti earthquake (Olson et al. 2011). Fig. 1 depicts schematically the global distributions of coral reefs, the corresponding peak ground acceleration (PGA) levels with a 10% probability of exceedance in 50 years (Shedlock et al. 2000), the locations of observed coral sand liquefaction manifestations, and the locations of the coral sands for which laboratory investigations were conducted (Hyodo et al. 1998; Morioka and Nicholson 2000; Mao and Fahey 2003; Sharma and Ismail 2006; Brandes 2011; Sandoval and Pando 2012; Salem et al. 2013; Giretti et al. 2018; Zhou et al. 2019,

[1]Professor, Institute of Geotechnical Engineering, Nanjing Tech Univ., Nanjing 210009, China; Director, Civil Engineering and Earthquake Disaster Prevention Center of Jiangsu Province, Nanjing 210009, China (corresponding author). Email: gxc6307@163.com

[2]Ph.D. Student, Institute of Geotechnical Engineering, Nanjing Tech Univ., Nanjing 210009, China.

[3]Ph.D. Student, Institute of Geotechnical Engineering, Nanjing Tech Univ., Nanjing 210009, China.

[4]Associate Professor, Institute of Geotechnical Engineering, Nanjing Tech Univ., Nanjing 210009, China.

[5]Professor, Dept. of Civil Engineering, The Univ. of Hong Kong, Hong Kong.

2020; Rasouli et al. 2020). The high seismic intensity of the region poses a challenging issue in maintaining the safety of the ports and other infrastructure systems. From the geotechnical point of view, the undrained behavior of coral sand subjected to cyclic loadings associated with earthquake events is a critical concern.

The undrained response of granular soils subjected to cyclic loadings associated with earthquake events, especially the phenomenon of liquefaction, has been a problem of long-standing interest. However, most previous studies have focused on the symmetric cyclic loading condition, which is not applicable to slopes and embankments during earthquakes (Fig. 2). In a slope, the inclination (α_0) of the initial major principal stress to the vertical direction may continuously rotate from 0° to 90°, which can be an important issue in slope stability analysis. Furthermore, sandy soils usually exhibit direction-dependent mechanical behavior due to their inherent anisotropic fabric, and their undrained responses also depend on the cyclic loading patterns. The influence of anisotropy on the liquefaction resistance has always been a concern (e.g., Oda et al. 1985; Yang and Sze 2011a; Sivathayalan et al. 2015; Georgiannou et al. 2018; Chen et al. 2020b). Different factors for correcting the liquefaction resistance of anisotropically consolidated saturated sandy soils have been proposed to consider the effect of static shear stress (usually referred to as the anisotropic consolidation path and stress ratio) (e.g., Harder and Boulanger 1997; Boulanger 2003; Yang and Sze 2011b; Wei and Yang 2019). Georgiannou et al. (2018) showed that the anisotropic consolidation significantly affected the undrained responses and the mobilized effective angle of shear resistance at the phase transformation state was closely related to the intermediate principal stress coefficient (b) and the rotation of principal stress. Meanwhile, the results of isotropically consolidated undrained cyclic shear tests indicated that the influence of principal stress rotation level on the liquefaction resistance of a loose sand is much stronger than that of the principal stress rotation pattern, while the feature of cyclic shear stress on the bedding plane is more important than the

© ASCE 04021093-1 J. Geotech. Geoenviron. Eng.

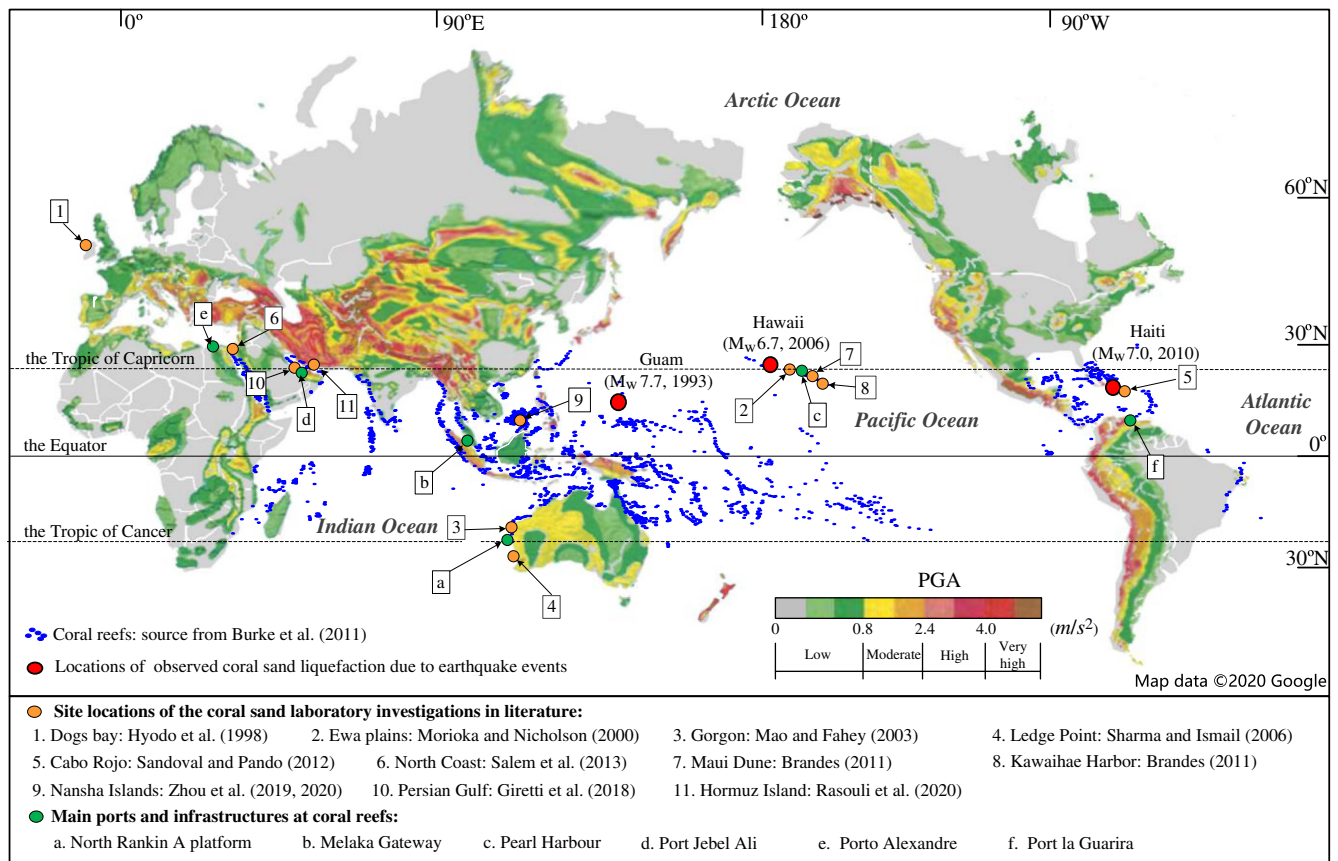J. Geotech. Geoenviron. Eng., 2021, 147(9): 04021093

Fig. 1. Map showing global distributions of coral reefs, locations of coral sand liquefaction sites, and seismic hazard levels. (Base map data © 2020 Google.)

orientation of the major principal stress along the bedding plane (Sivathayalan et al. 2015). Wei and Yang (2019) performed undrained cyclic triaxial tests to investigate the liquefaction resistance of silty sands with varying initial static shear stress levels, and quantified the influence of initial static shear stress levels on the liquefaction resistance using the initial state parameter in the framework of critical state soil mechanics. Most recently, the systematic undrained cyclic shear tests (maintaining a constant value of $b = 0.5$) of Chen et al. (2020b) revealed the influence of the pattern and level of principal stress rotation on the excess pore water pressure generation and liquefaction resistance of a silt soil.

Note that most of the previous experimental studies focused mainly on siliceous sands. The undrained anisotropic behavior and liquefaction resistance of coral sands are not yet well studied, and, particularly, the coupled effects of anisotropic consolidation and principal stress rotation pattern remain unclear. Table 1 summarizes the index properties of various coral sands reported in literature. Most of the laboratory tests were undrained cyclic simple shear (UCSS) tests or undrained cyclic triaxial (UCTX) tests, except that Zhou et al. (2019, 2020) performed a limited number of undrained cyclic torsional shear (UCTS) tests on coral sand specimens under the 90° jump of principal stress.

The present paper reports a comprehensive experimental study to investigate the undrained anisotropy and liquefaction susceptibility of a coral sand subjected to both the 90° jump and the continuous rotation of principal stresses. The laboratory experiments covered a reasonably wide range of consolidation ratio k_c (relating to the initial static shear stress level) and α_0 (relating to the

anisotropic consolidation path) values. A number of undrained monotonic shear tests with different shear loading paths were also conducted at various k_c and α_0 values, and the results can be used as benchmarks in the analysis of undrained anisotropic behavior. In all the undrained monotonic and cyclic shear tests, the intermediate principal stress coefficient (b) was maintained at a constant of 0.5 to eliminate the influence of varying b values during the loading process.

Test Apparatus, Materials, and Program

Testing Materials

The tested coral sand was taken from a coral reef in the Nansha Islands, South China Sea. It is composed of approximately 55.5% aragonite, 41.5% high-magnesian calcite, and 3.0% calcite. The coral sand particles have rough surfaces and numerous intraparticle pores, and their shapes are very irregular, mostly flaky and angular. The roundness and sphericity of the particles, estimated by visual comparison of the shapes of ~30 particles with the reference shapes, are 0.21 and 0.65, respectively. Fig. 3 shows the scanning electron microscope images of the grains and the particle size distribution of the tested coral sand. For comparison, the particle size distributions of Fujian sand (i.e., the Chinese standard siliceous sand) and nonplastic Nantong silt (Chen et al. 2020b) are also shown in Fig. 3. Note that the particle size distribution of Fujian sand was scaled to be the same as the tested coral sand in order to remove the potential influence of gradation. The roundness and

© ASCE 04021093-2 J. Geotech. Geoenviron. Eng.

J. Geotech. Geoenviron. Eng., 2021, 147(9): 04021093
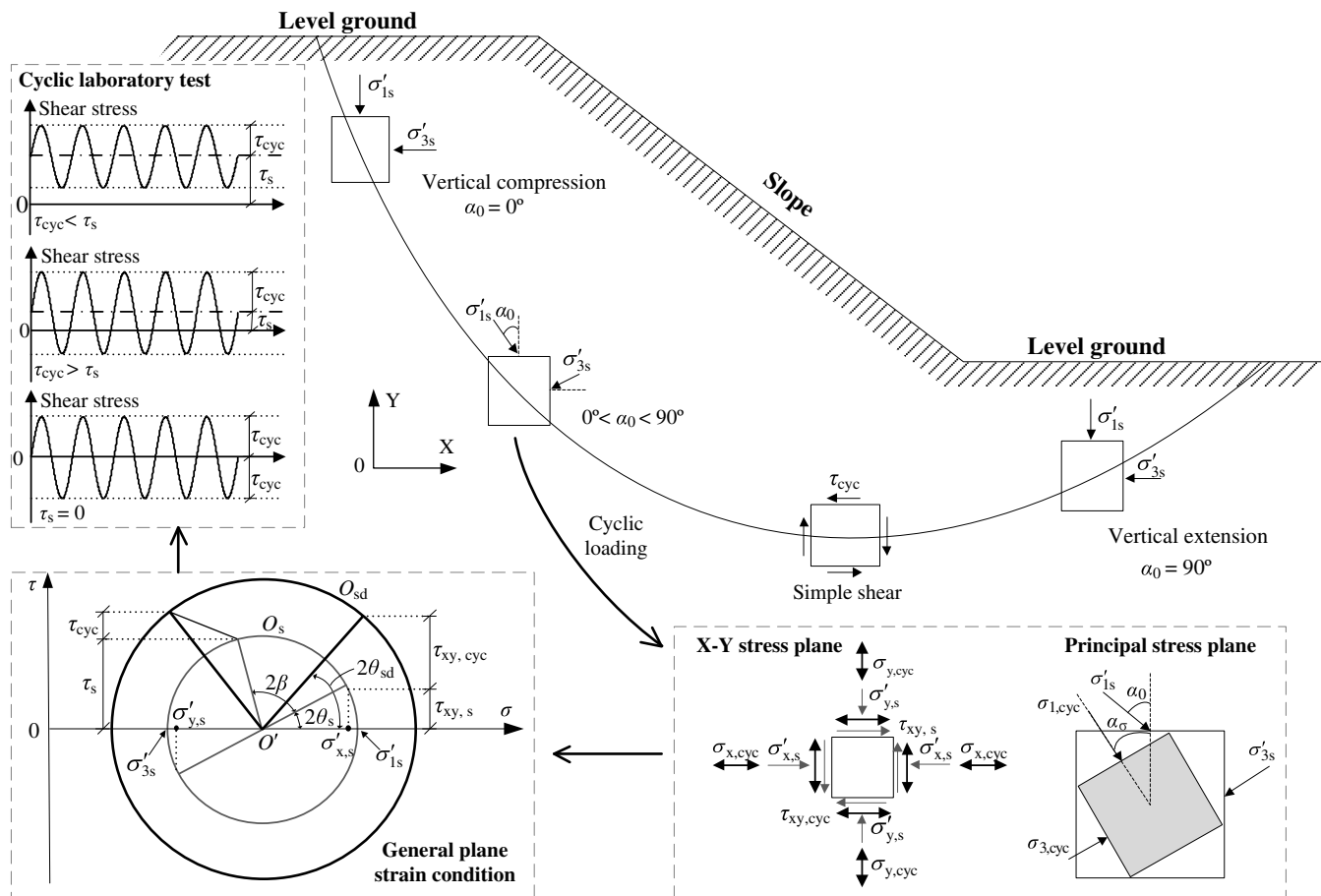
NOTE : subscript c denotes static stress; subscript cyc denotes cyclic stress; σ = normal stress; τ = shear stress; O_s = Mohr's circle of effective static stresses; O_{sd} = Mohr's circle of synthesizing static and cyclic stresses; O' = Mohr's circle center; θ_s = the orientation of the major principal stress plane of static stresses to the X axis; θ_{sd} = the orientation of the major principal stress plane of synthesizing static and cyclic stresses to the X axis; and β = the orientation of the maximum cyclic shear plane.

Fig. 2. Stress states of soil elements in sloping ground subjected to horizontal earthquake motion and the laboratory cyclic shear tests to simulate the stress states.

Table 1. Experimental studies on liquefaction susceptibility of coral sand reported in the literature

Number	Site location	Index property						CaCO$_3$ (%)	Group symbol[a]	Test category	Reference
		G_s	e_{min}	e_{max}	d_{50}	C_u	C_c				
1	Dogs Bay	2.72	1.62	2.45	0.23	2.52	0.99	88–94	SP	UCTX	Hyodo et al. (1998)
2	Ewa Plains	2.72	0.66	1.30	0.77	5.04	0.97	98	SP	UCTX	Morioka and Nicholson (2000)
3	Goodwyn	2.72	1.27	2.32	0.13	11.08	1.89	94	SM	UCTX	Sharma and Ismail (2006)
4	Ledge Point	2.76	0.90	1.21	0.20	1.83	0.92	91	SP		
5	Maui Dune	2.76	0.61	0.83	0.37	2.69	0.79	100	SP	UCSS	Brandes (2011)
6	Kawaihae Harbor	2.75	0.64	1.05	0.72	43.41	0.47	100	SM		
7	Cabo Rojo	2.84	1.51	2.07	0.37	1.74	0.94	91	SP	UCTX	Sandoval and Pando (2012)
8	North Coast	2.79	0.75	1.04	0.31	2.40	1.01	99	SP-SM	UCTX	Salem et al. (2013)
9	Persian Gulf	2.81	0.54	0.95	0.34	5.58	0.82	91	SP-SM	UCTX	Giretti et al. (2018)
10	Hormuz island	2.73	0.56	0.88	0.31	1.80	0.87	92	SP	UCSS	Rasouli et al. (2020)
11	South China Sea	2.73	1.02	1.44	0.39	3.55	0.97	90.25	SP	UCTS	Zhou et al. (2019)
12										UCTS	Zhou et al. (2020)

Note: G_s = specific gravity; e_{max} and e_{min} = maximum and minimum void ratios, respectively; d_{50} = mean particle size; C_u = coefficient of uniformity; C_c = curvature coefficient; and CaCO$_3$ = calcium carbonate content.

[a]Group symbol is determined following the Unified Soil Classification System.

sphericity of the rounded Fujian sand particles were 0.69 and 0.74, respectively. The basic index properties of coral sand and Fujian sand, determined following the ASTM standards, are listed in Table 2. Following the Unified Soil Classification System (ASTM 2011), the experimental coral sand and Fujian sand are classified as poorly graded sand (SP). The basic properties of Nantong silt and the experimental data used below can be found in Chen et al. (2020b).
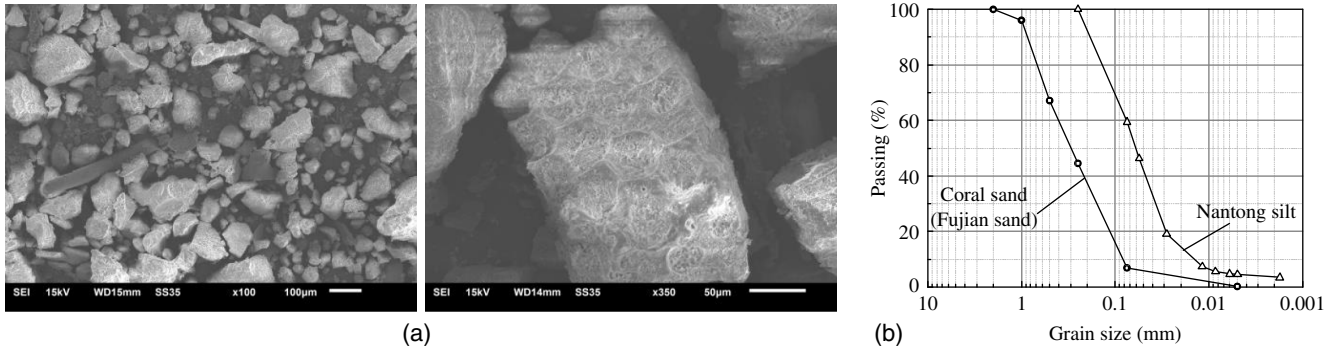
© ASCE   04021093-3   J. Geotech. Geoenviron. Eng.

J. Geotech. Geoenviron. Eng., 2021, 147(9): 04021093

Fig. 3. (a) Scanning electron micrographs of coral sand; and (b) grain size distributions of coral sand, Fujian sand, and Nantong silt (data from Chen et al. 2020b.)

Table 2. Index properties of coral sand and Fujian sand used in the tests

Characteristics	Value	
	Coral sand	Fujian sand
Mean particle size, d_{50} (mm)	0.31	0.31
Coefficient of uniformity, $C_u = d_{60}/d_{10}$	4.67	4.67
Curvature coefficient, $C_c = d_{30}^2/(d_{10}d_{60})$	0.86	0.86
Specific gravity, G_s	2.80	2.65
Maximum void ratio, e_{max}	1.72	0.75
Minimum void ratio, e_{min}	0.99	0.41

Note: d_{10}, d_{30}, d_{50}, and d_{60} are the particle sizes corresponding to 10%, 30%, 50%, and 60% finer on the cumulative particle size distribution curve, respectively.

Testing Apparatus and Principle

An advanced hollow cylinder torsional apparatus (HCTA) manufactured by GDS Instruments (Hook, Hampshire, United Kingdom) is used for the undrained monotonic and cyclic shear tests in this study. The details of the test apparatus can be found in Chen et al. (2020a). The axial force (W) (or axial displacement), torque (M_T), outer cell pressure (p_o), and inner cell pressure (p_i) can be dynamically and independently controlled [Fig. 4(a)]. The stress components [vertical (axial) stress σ_z, radial stress σ_r, circumferential stress σ_θ, and torsional shear stress $\tau_{z\theta}$] and the corresponding major, intermediate, and minor principal stresses σ_1, σ_2, and σ_3 acting on the thin wall of a hollow cylindrical soil specimen are schematically shown in Figs. 4(b and c), respectively. For cyclic loadings, waveform functions of $W(t)$, $M_T(t)$, $p_i(t)$, and $p_o(t)$ can be implemented and controlled in the HCTA. Table 3 lists the equations to determine the four waveform functions and the stress variables of p, q, α, and b, where p and q are the mean principal stress and deviatoric stress, respectively; α is the major principal stress orientation with respect to the vertical direction; and b is the intermediate principal stress coefficient. To minimize the stress nonuniformity in the hollow cylindrical specimen, the value of p_i/p_o should be maintained in a limited range, such as between 0.83 and 1.11 (Hight et al. 1983), between 0.75 and 1.3 (Nakata et al. 1998), or between 0.90 and 1.01 (Chen et al. 2020b). In this study, the value of p_i/p_o was maintained in the range from 0.98 to 1.02.

Membrane penetration is a well-known limitation in cyclic shear tests, and it may increase the resistance of granular soils, especially for very coarse granular soils (Chen et al. 2021b). Fig. 5(a) shows the photographs of a coral sand specimen and a gravel specimen after consolidation. The mean grain size of the tested coral sand
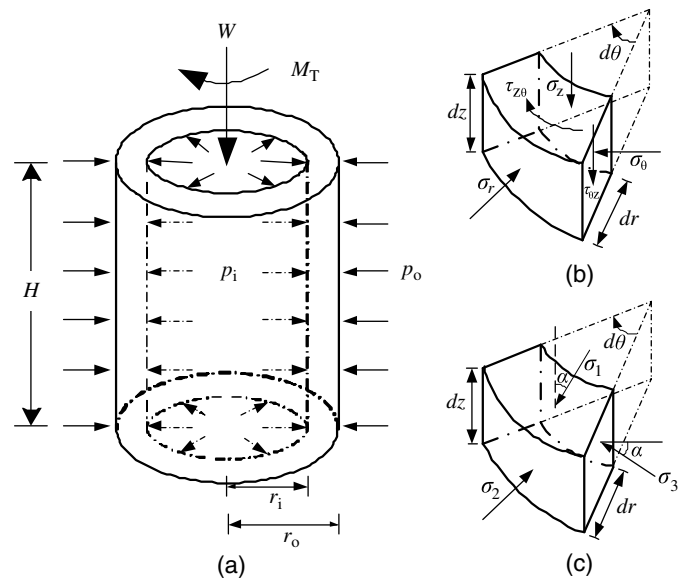

Fig. 4. Illustrative stress state in a hollow cylindrical specimen subjected to axial load W, torque M_T, inner pressure p_i, and outer pressure p_o: (a) applied loads; (b) stress components; and (c) principal stress components.

is 0.31 mm, while the particle size of the gravel is in the range of 5–10 mm. Membrane penetration can be clearly observed in the gravel specimen, but hardly in the coral sand specimen, suggesting that the membrane penetration effect may be ignored.

To further clarify this point, additional cyclic loading tests were performed to quantify the stress-induced by the membrane. The tests were performed on water specimens (i.e., the tested material is water). Cyclic loading was applied at the double amplitude shear strain of 6% or the axial strain level of 6%. Figs. 5(b and c) show the stress-strain curves associated with the membrane for vertical (axial) and torsional shear loading, respectively. It is noted that at the axial strain (ε_z) or shear strain ($\gamma_{z\theta}$) level of 2.5%, the values of σ_z and $\tau_{z\theta}$ are less than 1 kPa, confirming that the membrane effect is negligible.

Fig. 6 illustrates the typical undrained responses (the curves of excess pore water pressure u_e; strain components ε_z, ε_r, ε_θ, and $\gamma_{z\theta}$; generalized shear strain γ_g; and b value plotted against the number of cycles N, respectively; stress paths of q versus effective mean principal stress p' and $\tau_{z\theta}$ versus $(\sigma_z - \sigma_\theta)/2)$ of isotropically

© ASCE 04021093-4 J. Geotech. Geoenviron. Eng.

J. Geotech. Geoenviron. Eng., 2021, 147(9): 04021093

Table 3. Equations for data interpretation

Component	Stress	Strain	Stress state variable	Waveform function
Vertical	$\sigma_z = \dfrac{W}{\pi(r_o^2 - r_i^2)} + \dfrac{p_o r_o^2 - p_i r_i^2}{(r_o^2 - r_i^2)}$	$\varepsilon_z = \dfrac{z}{H}$	Intermediate principal stress coefficient $b = (\sigma_2 - \sigma_3)/(\sigma_1 - \sigma_3)$	—
Radial	$\sigma_r = \dfrac{p_o r_o + p_i r_i}{r_o + r_i}$	$\varepsilon_r = -\dfrac{u_o - u_i}{r_o - r_i}$	Inclination of major principal stress $\alpha = \arctan(2\tau_{\theta z}/(\sigma_z - \sigma_\theta))/2$	—
Circumferential	$\sigma_\theta = \dfrac{p_o r_o - p_i r_i}{r_o - r_i}$	$\varepsilon_\theta = -\dfrac{u_o + u_i}{r_o + r_i}$	Mean principal stress $p = (\sigma_1 + \sigma_2 + \sigma_3)/3$	—
Shear	$\tau_{z\theta} = \dfrac{3M_T}{2\pi(r_o^3 - r_i^3)}$	$\gamma_{z\theta} = \dfrac{2\theta(r_o^3 - r_i^3)}{3H(r_o^2 - r_i^2)}$	—	$W(t) = q(t)\pi(r_o^2 - r_i^2)\left(\dfrac{1 - 2b}{2} + \dfrac{3}{2}\cos(2\alpha(t))\right)$ $M_T(t) = \dfrac{2\pi(r_o^3 - r_i^3)}{3}q(t)\sin(2\alpha(t))$
Major principal	$\sigma_1 = \dfrac{\sigma_z + \sigma_\theta}{2} + \sqrt{\left(\dfrac{\sigma_z - \sigma_\theta}{2}\right)^2 + \tau_{z\theta}^2}$	$\varepsilon_1 = \dfrac{\varepsilon_z + \varepsilon_\theta}{2} + \sqrt{\left(\dfrac{\varepsilon_z - \varepsilon_\theta}{2}\right)^2 + \gamma_{z\theta}^2}$		$p_o(t) = \dfrac{m}{r_o}q(t) - \dfrac{r_o - r_i}{2r_o}q(t)\cos(2\alpha(t)) + p$
Intermediate principal	$\sigma_2 = \sigma_r$	$\varepsilon_2 = \varepsilon_r$		$p_i(t) = \dfrac{n}{r_i}q(t) + \dfrac{r_o - r_i}{2r_i}q(t)\cos(2\alpha(t)) + p$
Minor principal	$\sigma_3 = \dfrac{\sigma_z + \sigma_\theta}{2} - \sqrt{\left(\dfrac{\sigma_z - \sigma_\theta}{2}\right)^2 + \tau_{z\theta}^2}$	$\varepsilon_3 = \dfrac{\varepsilon_z + \varepsilon_\theta}{2} - \sqrt{\left(\dfrac{\varepsilon_z - \varepsilon_\theta}{2}\right)^2 + \gamma_{z\theta}^2}$		$m = (r_o + r_i)\dfrac{2b - 1}{3} - (r_o - r_i)\dfrac{2b - 1}{6}$
Deviatoric	$q = (\sigma_1 - \sigma_3)/2$	$\gamma_q = \varepsilon_1 - \varepsilon_3$		$n = (r_o + r_i)\dfrac{2b - 1}{3} + (r_o - r_i)\dfrac{2b - 1}{6}$
Generalized	$q_g = \sqrt{\dfrac{1}{2}[(\sigma_1 - \sigma_2)^2 + (\sigma_1 - \sigma_3)^2 + (\sigma_2 - \sigma_3)^2]}$	$\gamma_g = \dfrac{\sqrt{2}}{3}\sqrt{(\varepsilon_1 - \varepsilon_2)^2 + (\varepsilon_1 - \varepsilon_3)^2 + (\varepsilon_2 - \varepsilon_3)^2}$		

Note: r_o = outer radius; r_i = inner radius; H = height of specimen; z = axial deformation; u_o and u_i = radial deformations of the outer and inner walls calculated from the change of inner and outer volumes, respectively; θ = torsional deformation; b = intermediate principal stress coefficient; and α = orientation of the σ_1 axis to the vertical.
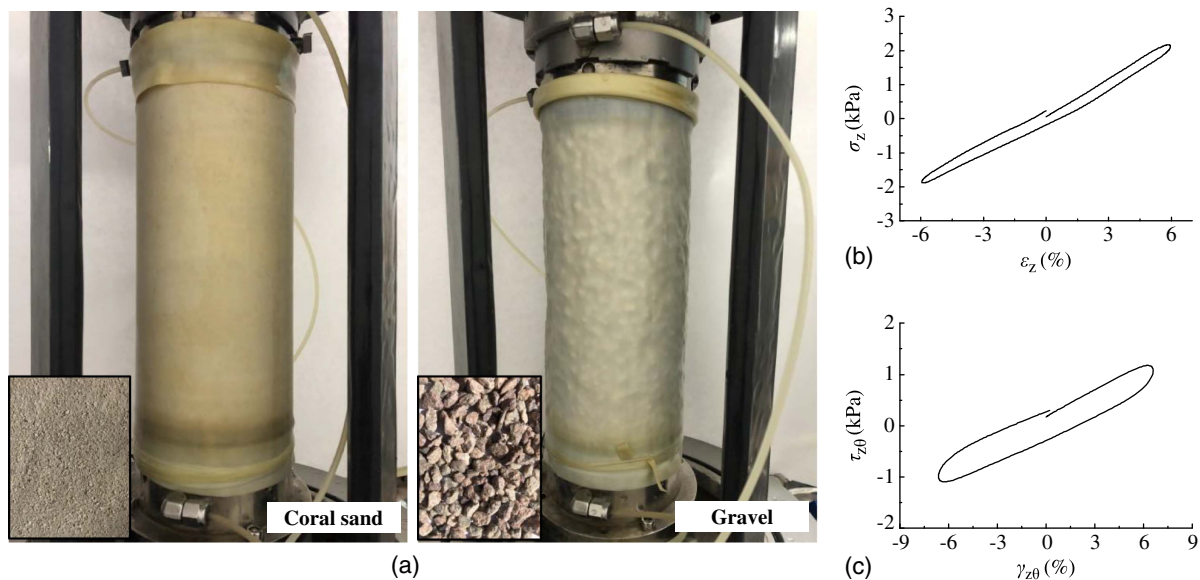
Fig. 5. (a) Photographs of coral sand specimen and gravel specimen; (b) measured vertical stress-strain curve associated with membrane; and (c) measured torsional shear stress-strain curve associated with membrane.

consolidated saturated coral sand and Fujian sand specimens subjected to the 90° jump or the continuous rotation of principal stress, as well as the results of Nantong silt from Chen et al. (2020b). The b values in the undrained cyclic shear tests are quite consistent with the target value of 0.5. Thus, the actual stress paths in the undrained cyclic shear tests agree well with the expected ones, as shown in Fig. 6(h).

Specimen Preparation, Saturation, and Consolidation

The height, outer diameter, and inner diameter of the hollow cylinder specimens tested are 200, 100, and 60 mm, respectively. Because the specimen preparation method significantly affects the undrained response of sand (Sze and Yang 2014), a dry deposition method similar to the one used by Chen et al. (2020b) was used to prepare the specimens in this study. In this method, the specimen was prepared in seven layers and the oven-dried coral sand was placed using a funnel with zero falling head. A compaction device was applied on the specimen to ensure that each layer could achieve the target initial relative density $D_r = 45\%$. To compensate for the influence of the upper layer being placed on the lower layer, making densification likely, the layer masses were decreased about 1% from top to bottom. After consolidation, the actual relative densities D_{rc} vary between 48.16% and 52.73%, as listed in Tables 4–6. Note that the subscript c in this paper denotes after consolidation.

The saturation and consolidation processes for all specimens followed the ASTM standard (ASTM 2013). After being placed in the chamber, the specimen was carefully flushed first with carbon dioxide and then with de-aired water. The specimen was then back-pressurized to 400 kPa, with a Skempton B-value of 0.97 or higher for complete saturation. After saturation, each specimen was isotropically or anisotropically consolidated along the stress paths in Fig. 7(b) to reach an initial effective mean principal stress $p_0' = 100$ kPa, and total mean principal stress p is maintained at a constant of 500 kPa.

Undrained Monotonic Shear Tests

A series of undrained monotonic shear tests were performed to better understand the influence of stress paths on the undrained

anisotropy of saturated coral sand and provide benchmarks for evaluating the undrained cyclic shear feature. Table 4 lists the details of the undrained monotonic shear test program. In Table 4, the consolidation stress ratio $k_c = \sigma_{1c}'/\sigma_{3c}'$, where σ_{1c}' and σ_{3c}' are the initial effective major and minor principal stresses at the end of consolidation, respectively. Fig. 7(c) depicts the stress paths during undrained monotonic shear tests, in which α_m is the inclination of monotonic shear loading to the vertical axis [Fig. 7(a)]. For each consolidation condition, five specimens were monotonically sheared at five fixed α_m values, as shown in Fig. 7(c).

Undrained Cyclic Shear Tests

After consolidation, undrained cyclic shear tests were performed, and the cyclic deviator stresses were sinusoidal with a frequency of 0.5 Hz. For the 90° jump of principal stress tests, the stress paths in the deviatoric stress plane are schematically explained in Fig. 8, in which α_σ quantifies the initial direction of a sequence of cyclic loading deviating from the vertical axis. For the continuous rotation of principal stress tests, the stress paths in the deviatoric stress plane are schematically explained in Fig. 9, in which $\alpha_{\sigma\max}$ quantifies the maximum inclination of a sequence of cyclic loading to the vertical axis. More details about the cyclic stress paths of the 90° jump and the continuous rotation of principal stress can be found in Chen et al. (2020b). Tables 5 and 6 list the detailed test programs for the 90° jump and the continuous rotation of principal stress tests, respectively. In these tables, CSR is the conventional cyclic stress ratio, which is defined as the ratio of the cyclic deviatoric stress amplitude q_{am} to the p_0'.

Test Results and Analysis

Undrained Monotonic Shear Responses

Fig. 10 shows the effective stress paths in the q-p' plane for the coral sand specimens in undrained monotonic shear tests. It is noted that the influences of α_0 and α_m on the undrained monotonic shear response of the coral sand are significant. The value of p' for all specimens decreases first with increasing q, accompanied by
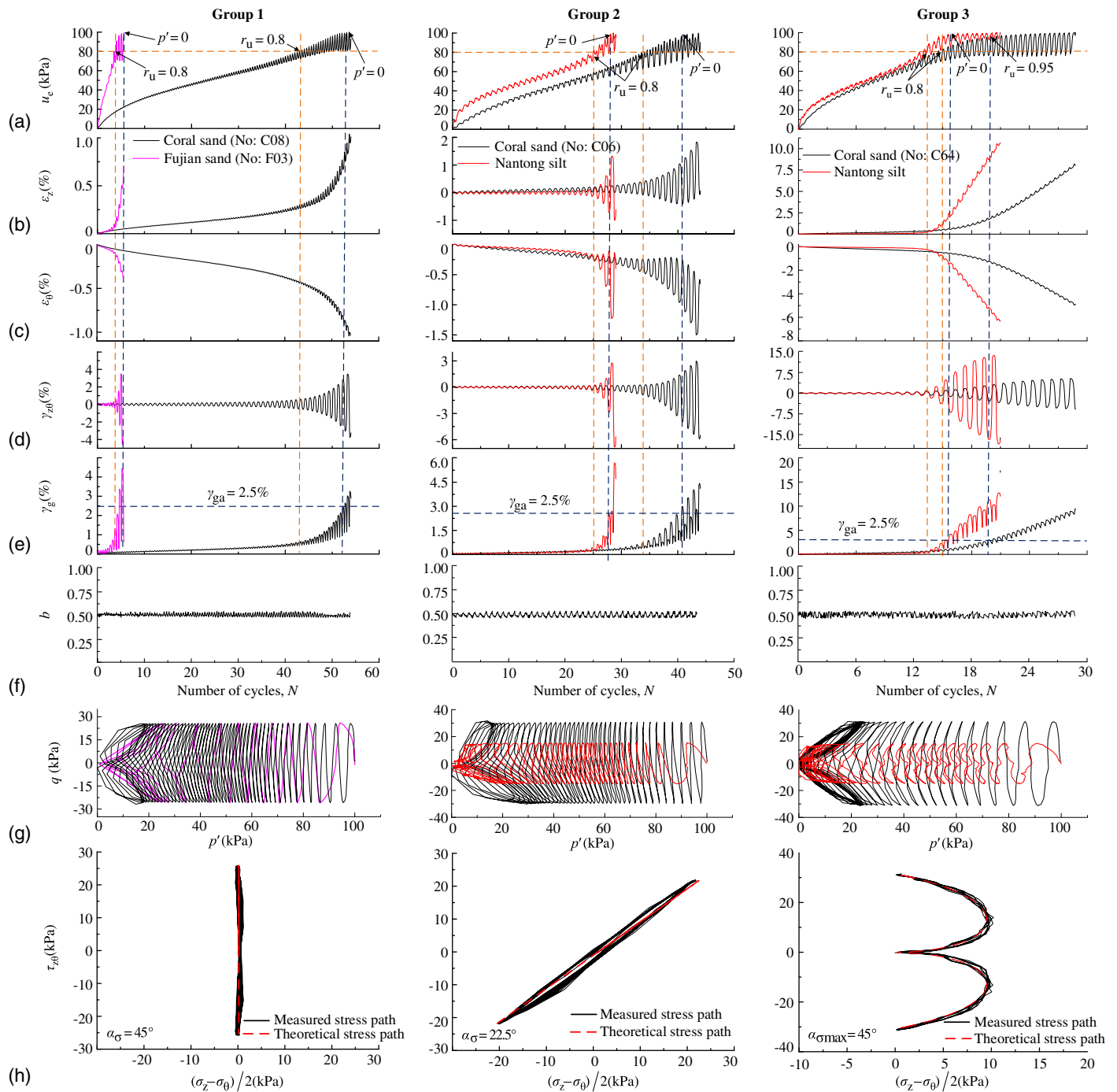
Fig. 6. Undrained cyclic shear response of coral sand, Fujian sand, and Nantong silt specimens subjected to the 90° jump of principal stress (Groups 1 and 2) and to the continuous rotation of principal stress (Group 3): (a) u_e versus N; (b) ε_z versus N; (c) ε_θ versus N; (d) $\gamma_{z\theta}$ versus N; (e) γ_g versus N; (f) b versus N; (g) effective stress paths; and (h) stress path of $\tau_{z\theta}$ versus $(\sigma_z - \sigma_\theta)/2$.

contraction until a limiting q value at the phase transformation state, after which p' continuously increases with increasing q, accompanied by dilation. The soil behavior changes from contraction to dilation at the phase transformation state, and this feature is independent of the monotonic loading directions and the consolidation conditions. Therefore, the dilative behavior in the undrained monotonic shear tests is an inherent behavior of the coral sand due to irregular particle shape and the presence of numerous intraparticle pores, regardless of α_0 and α_m values. On the contrary, Sivathayalan and Vaid (2002) showed that that Fraser River sand

in the undrained monotonic shear tests exhibited full contraction behaviors by inclining the principal stress orientations toward bedding layers. This is one of the prominent differences between the coral sand and the siliceous sand under various orientations of principal stress. Fig. 10 also shows the mobilized shear resistance S_{PT} at the phase transformation state (i.e., q value corresponding to the minimum value of p') and the corresponding effective friction angle (ϕ'_{PT}). For isotropically consolidated cases, the variation of S_{PT} with increasing α_m from 0° to 90° is an upward-bending parabola trend, and the S_{PT} along the inclination of $\alpha_m = 45°$ is the lowest,

© ASCE 04021093-7 J. Geotech. Geoenviron. Eng.

J. Geotech. Geoenviron. Eng., 2021, 147(9): 04021093

Table 4. Scheme of undrained monotonic shear tests

Test group	Test ID	End of consolidation ($p = 500$ kPa, $p_0' = 100$ kPa)				Parameters during testing	
		b_0	k_c	α_0 (degrees)	D_{rc} (%)	b_m	α_m (degrees)
UM1	M01	—	1.0	—	51.04	0.5	0
	M02				50.82		22.5
	M03				50.94		45
	M04				51.63		67.5
	M05				50.84		90
UM2	M06	0.5	1.5	0	51.64	0.5	0
	M07				51.38		22.5
	M08				51.81		45
	M09				50.83		67.5
	M10				50.58		90
UM3	M11	0.5	1.5	45	50.35	0.5	0
	M12				50.80		22.5
	M13				51.13		45
	M14				50.40		67.5
	M15				50.43		90
UM4	M16	0.5	1.5	90	49.86	0.5	0
	M17				49.84		22.5
	M18				50.26		45
	M19				50.24		67.5
	M20				50.89		90

while ϕ_{PT}' decreases linearly as α_m increases. For anisotropically consolidated cases, the variations of both S_{PT} and ϕ_{PT}' with α_m are quite complex and significantly affected by α_0. It is interesting to find that the shear resistance S_{PT} along the inclination of consolidation path (i.e., $\alpha_m = \alpha_0$) is largest.

It convincingly indicates that the undrained monotonic shear behaviors of the coral sand tested significantly depend on the stress paths of anisotropic consolidation and monotonic shearing due to its inherent anisotropy.

Undrained Cyclic Responses

Undrained Cyclic Response Features and Failure Criterion
The liquefaction mechanism and resistance of coral sand, particularly under the complex loading patterns and anisotropic consolidations, are of considerable interest but are not well understood. Fig. 6 illustrates the undrained cyclic responses of isotropically consolidated coral sand and Fujian sand in this study, and Nantong silts in Chen et al. (2020b) subjected to the 90° jump or the continuous rotation of principal stress. As shown in Fig. 6(g), the cyclic deviatoric stress reverses during the undrained cyclic shearing due to the initial isotropic consolidation stress state. The u_e generation rate in coral sand is significantly lower than those in Fujian sand and Nantong silt, even though the CSR applied on coral sand is higher than those applied on Fujian sand and Nantong silt. For

Table 5. Information on undrained cyclic shear tests for 90° jump of principal stress

Test group	Test ID	End of consolidation ($p = 500$ kPa, $p_0' = 100$ kPa)				Parameters during undrained cyclic shear testing ($b_\sigma = 0.5$)				
		b_0	k_c	α_0 (degrees)	D_{rc} (%)	α_σ (degrees)	CSR	$u_{e2.5}/p_0'$	D_1	D_2
CJ1	C01	—	1.0	—	50.61	$0 \leftrightarrow 90$	0.20	1.00	1.00	1.00
	C02				49.68	$0 \leftrightarrow 90$	0.25	1.00		
	C03				51.40	$0 \leftrightarrow 90$	0.30	0.98		
	C04				51.99	$22.5 \leftrightarrow -67.5$	0.20	0.98		
	C05				51.78	$22.5 \leftrightarrow -67.5$	0.25	0.98		
	C06				51.89	$22.5 \leftrightarrow -67.5$	0.30	0.99		
	C07				51.63	$45 \leftrightarrow -45$	0.20	0.98		
	C08				52.26	$45 \leftrightarrow -45$	0.25	0.99		
	C09				51.59	$45 \leftrightarrow -45$	0.30	0.98		
	C10				51.44	$67.5 \leftrightarrow -22.5$	0.20	0.98		
	C11				51.13	$67.5 \leftrightarrow -22.5$	0.25	0.99		
	C12				51.12	$67.5 \leftrightarrow -22.5$	0.30	0.99		
	C13				50.53	$90 \leftrightarrow 0$	0.25	1.00		
	C14				51.30	$90 \leftrightarrow 0$	0.30	1.00		
	C15				51.54	$90 \leftrightarrow 0$	0.35	1.00		
CF1	F01	—	1.0	—	49.12	$45 \leftrightarrow -45$	0.15	1.00	1.00	1.00
	F02				48.95	$45 \leftrightarrow -45$	0.20	1.00		
	F03				48.99	$45 \leftrightarrow -45$	0.25	1.00		
CJ2	C16	0.5	1.5	0	52.41	$0 \leftrightarrow 90$	0.25	0.93	1.16	0.99
	C17				52.22	$0 \leftrightarrow 90$	0.30	0.96		
	C18				51.28	$0 \leftrightarrow 90$	0.35	0.98		
	C19				51.36	$22.5 \leftrightarrow -67.5$	0.25	0.88		
	C20				51.35	$22.5 \leftrightarrow -67.5$	0.30	0.82		
	C21				51.49	$22.5 \leftrightarrow -67.5$	0.35	0.86		
	C22				51.77	$45 \leftrightarrow -45$	0.25	0.85		
	C23				52.02	$45 \leftrightarrow -45$	0.30	0.84		
	C24				52.73	$45 \leftrightarrow -45$	0.35	0.85		
	C25				51.95	$67.5 \leftrightarrow -22.5$	0.25	0.89		
	C26				51.47	$67.5 \leftrightarrow -22.5$	0.30	0.88		
	C27				51.85	$67.5 \leftrightarrow -22.5$	0.35	0.88		
	C28				51.91	$90 \leftrightarrow 0$	0.25	0.93		
	C29				51.75	$90 \leftrightarrow 0$	0.30	0.96		
	C30				52.41	$90 \leftrightarrow 0$	0.35	0.98		

Table 5. (*Continued.*)

Test group	Test ID	End of consolidation ($p = 500$ kPa, $p'_0 = 100$ kPa)				Parameters during undrained cyclic shear testing ($b_\sigma = 0.5$)				
		b_0	k_c	α_0 (degrees)	D_{rc} (%)	α_σ (degrees)	CSR	$u_{e2.5}/p'_0$	D_1	D_2
CJ3	C31	0.5	1.25	0	50.88	$45 \leftrightarrow -45$	0.30	0.91	1.09	1.00
	C32		1.75		50.27	$45 \leftrightarrow -45$	0.30	0.75	1.22	0.99
CJ4	C33	0.5	1.5	45	51.49	$0 \leftrightarrow 90$	0.25	0.78	1.00	0.98
	C34				51.46	$0 \leftrightarrow 90$	0.30	0.78		
	C35				52.39	$0 \leftrightarrow 90$	0.35	0.98		
	C36				52.01	$22.5 \leftrightarrow -67.5$	0.25	0.86		
	C37				52.34	$22.5 \leftrightarrow -67.5$	0.30	0.87		
	C38				51.40	$22.5 \leftrightarrow -67.5$	0.35	0.86		
	C39				52.10	$45 \leftrightarrow -45$	0.25	0.88		
	C40				52.34	$45 \leftrightarrow -45$	0.30	0.92		
	C41				52.40	$45 \leftrightarrow -45$	0.35	0.89		
	C42				51.73	$67.5 \leftrightarrow -22.5$	0.25	0.82		
	C43				52.53	$67.5 \leftrightarrow -22.5$	0.30	0.83		
	C44				52.61	$67.5 \leftrightarrow -22.5$	0.35	0.81		
	C45				51.64	$90 \leftrightarrow 0$	0.25	0.80		
	C46				51.71	$90 \leftrightarrow 0$	0.30	0.79		
	C47				51.30	$90 \leftrightarrow 0$	0.35	0.78		
CJ5	C48	0.5	1.5	90	50.89	$0 \leftrightarrow 90$	0.20	0.91	0.86	0.98
	C49				52.46	$0 \leftrightarrow 90$	0.25	0.93		
	C50				51.11	$0 \leftrightarrow 90$	0.30	0.92		
	C51				50.38	$22.5 \leftrightarrow -67.5$	0.20	0.83		
	C52				51.65	$22.5 \leftrightarrow -67.5$	0.25	0.85		
	C53				51.19	$22.5 \leftrightarrow -67.5$	0.30	0.82		
	C54				50.81	$45 \leftrightarrow -45$	0.20	0.79		
	C55				51.52	$45 \leftrightarrow -45$	0.25	0.84		
	C56				50.52	$45 \leftrightarrow -45$	0.30	0.80		
	C57				50.87	$67.5 \leftrightarrow -22.5$	0.20	0.87		
	C58				50.67	$67.5 \leftrightarrow -22.5$	0.25	0.86		
	C59				51.22	$67.5 \leftrightarrow -22.5$	0.30	0.79		
	C60				52.14	$90 \leftrightarrow 0$	0.20	0.88		
	C61				51.24	$90 \leftrightarrow 0$	0.25	0.91		
	C62				51.62	$90 \leftrightarrow 0$	0.30	0.94		

Note: C = coral sand; F = Fujian sand; $u_{e2.5}$ = stability amplitude of excess pore water pressure at $\gamma_{ga} = 2.5\%$; and D_1 and D_2 = coefficients in Eq. (19).

Table 6. Information on undrained cyclic shear tests for the continuous rotation of principal stress

Test group	Test ID	End of consolidation ($p = 500$ kPa, $p'_0 = 100$ kPa)				Parameters during undrained cyclic shear testing ($b_\sigma = 0.5$)				
		b_0	k_c	α_0 (degrees)	D_{rc} (%)	$\alpha_{\sigma max}$ (degrees)	CSR	$u_{e2.5}/p'_0$	D_1	D_2
CR1	C63	—	1	—	49.87	$22.5 \leftrightarrow -22.5$	0.30	0.92	1.00	1.00
	C64				49.66	$45 \leftrightarrow 45$		0.95	1.00	1.00
	C65				50.12	$67.5 \leftrightarrow -67.5$		1.00	1.00	1.00
	C66				50.33	$90 \leftrightarrow -90$		1.00	1.00	1.00
CR2	C67	0.5	1.5	0	50.72	$22.5 \leftrightarrow -22.5$	0.30	0.68	1.24	0.98
	C68				50.18	$45 \leftrightarrow 45$		0.80	1.19	0.99
	C69				50.77	$67.5 \leftrightarrow -67.5$		0.88	1.13	0.99
	C70				50.47	$90 \leftrightarrow -90$		0.98	1.09	1.00
CR3	C71	0.5	1.25	0	50.13	$45 \leftrightarrow 45$	0.30	0.88	1.11	1.00
	C72		1.75		50.36	$45 \leftrightarrow 45$		0.76	1.26	0.98
CR4	C73	0.5	1.5	45	50.57	$22.5 \leftrightarrow -22.5$	0.30	0.78	1.08	0.98
	C74				50.45	$45 \leftrightarrow 45$		0.90	1.03	0.98
	C75				51.08	$67.5 \leftrightarrow -67.5$		0.88	0.97	0.98
	C76				50.16	$90 \leftrightarrow -90$		0.78	0.93	0.97
CR5	C77	0.5	1.5	90	50.08	$22.5 \leftrightarrow -22.5$	0.30	0.94	0.93	1.00
	C78				50.30	$45 \leftrightarrow 45$		0.84	0.89	0.99
	C79				50.35	$67.5 \leftrightarrow -67.5$		0.74	0.83	0.98
	C80				49.78	$90 \leftrightarrow -90$		0.66	0.79	0.97

Note: C = coral sand; $u_{e2.5}$ = stability amplitude of excess pore water pressure at $\gamma_{ga} = 2.5\%$; and D_1 and D_2 = Coefficients in Eq. (19).
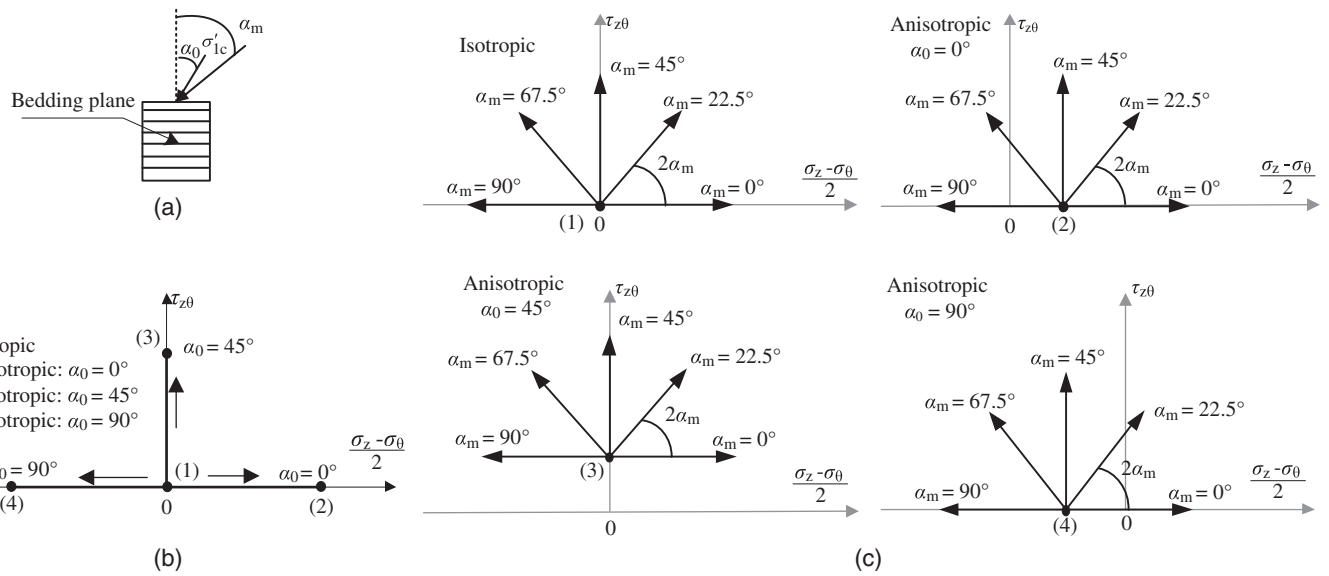
Fig. 7. (a) Inclination α_0 for consolidation and inclination α_m for monotonic shearing; (b) consolidation stress paths; and (c) monotonic shear stress paths.
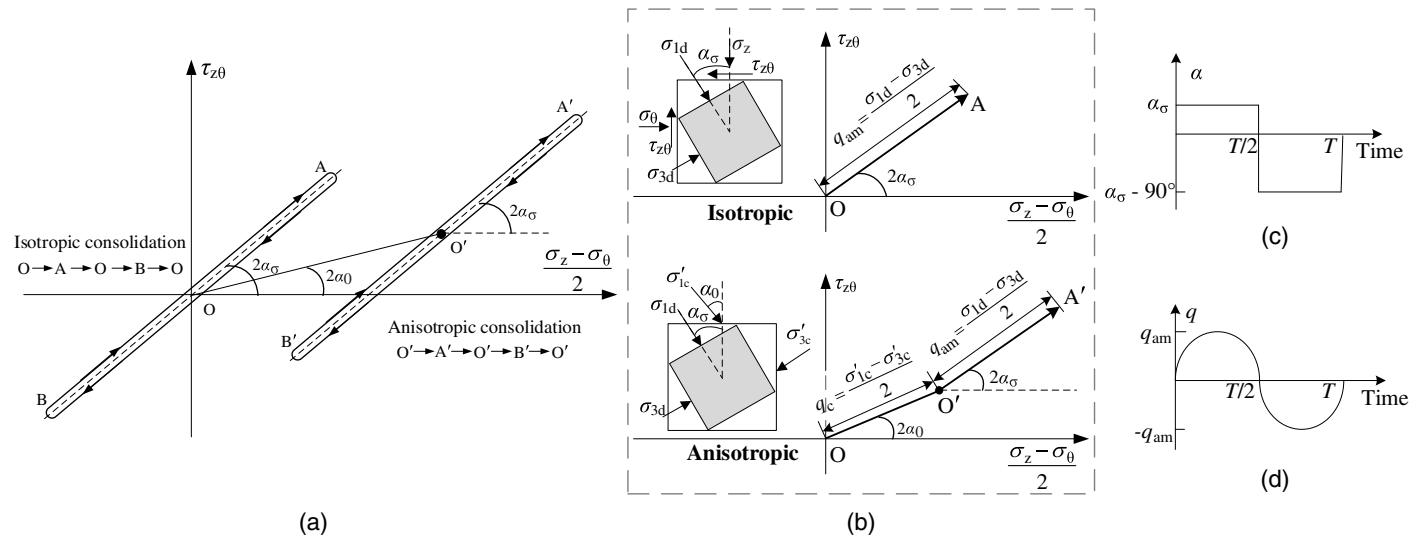

Fig. 8. Stress paths of cyclic loadings and stress state of soil element during the 90° jump of principal stress: (a) stress path; (b) stress state and local stress path; (c) α in one cycle; and (d) τ in one cycle.

Fujian sand and Nantong silt, the fluctuating amplitudes of ε_z, ε_r, ε_θ, $\gamma_{z\theta}$, and γ_g increase slowly until u_e reaches approximately $0.80p'_0$, after which the amplitudes increase rapidly at the subsequent cyclic loadings. Initial liquefaction occurred when $p' = 0$, resulting in larger strains. For coral sand, obvious fluctuation of strain components can be observed before u_e approaches $0.80p'_0$, after which the fluctuating amplitudes of various strain components increase. It was found that the coral sand needs a much larger number of cycles to trigger liquefaction than Fujian sand and Nantong silt. This phenomenon implies that the unique fabric of coral sand, such as the irregular particle shape (low sphericity) and the presence of numerous intraparticle pores, as well as its high $CaCO_3$ content, makes its undrained cyclic behaviors different from those of Fujian sand and Nantong silt. Note that the generalized shear strain amplitude $\gamma_{ga} = 2.5\%$ and the first transient

near-zero effective stress state for isotropically consolidated coral sand specimens occur almost simultaneously.

Fig. 11 compares the undrained strain responses of isotropically and anisotropically consolidated coral sand specimens subjected to the 90° jump of principal stress. A significant difference of the strain patterns exists between isotropically and anisotropically consolidated specimens under the same CSR (i.e., $CSR = 0.3$). Note that the initial static deviatoric stress for the anisotropically consolidated specimens plays a role as the driving force during the undrained cyclic shear loading, causing spontaneous axial compression and lateral bulging. Although the cyclic stress path and level during the undrained cyclic shear testing are identical (i.e., $\alpha_\sigma = 45°$, $CSR = 0.3$), the magnitude of the same strain component of various anisotropically consolidated specimens ($\alpha_0 = 0°$, 45°, and 90° at fixed $k_c = 1.5$) is still different, as shown in Figs. 11(b–d). For the

© ASCE   04021093-10   J. Geotech. Geoenviron. Eng.

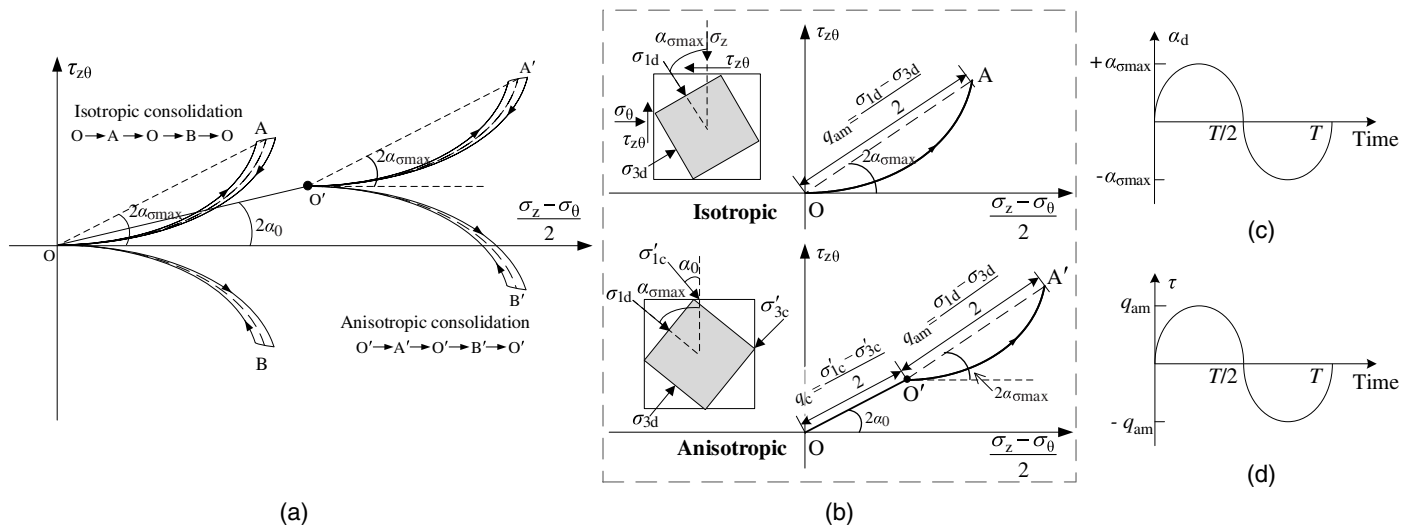J. Geotech. Geoenviron. Eng., 2021, 147(9): 04021093

Fig. 9. Stress paths of cyclic loadings and stress state of soil element during the continuous rotation of principal stress: (a) stress path; (b) stress state and local stress path; (c) α in one cycle; and (d) τ in one cycle.
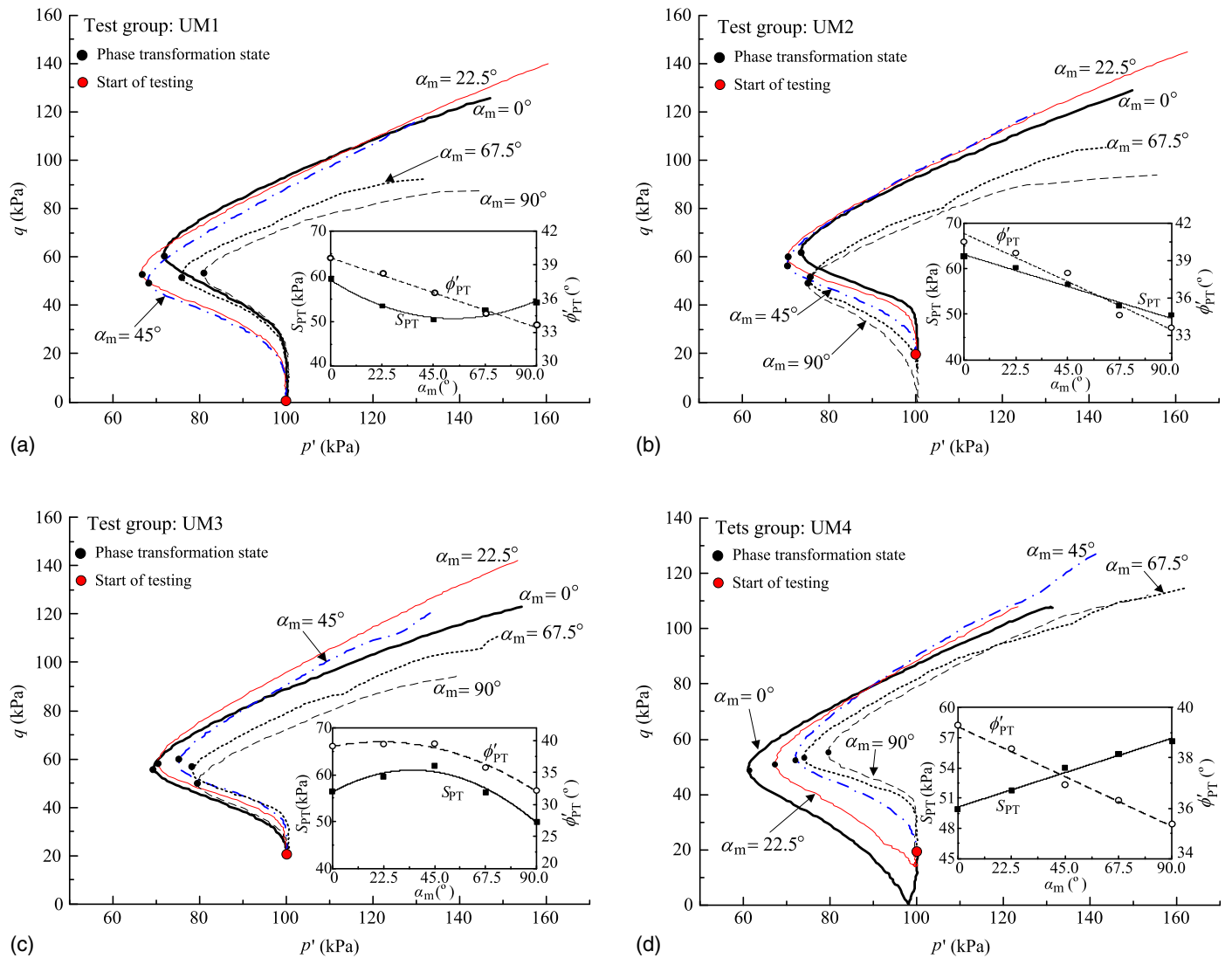

Fig. 10. Effective stress paths of saturated coral sand specimens during undrained monotonic shear tests: (a) isotropic consolidation; (b) anisotropic consolidation at $\alpha_0 = 0°$ and $k_c = 1.5$; (c) anisotropic consolidation at $\alpha_0 = 45°$ and $k_c = 1.5$; and (d) anisotropic consolidation at $\alpha_0 = 90°$ and $k_c = 1.5$.

© ASCE   04021093-11   J. Geotech. Geoenviron. Eng.

J. Geotech. Geoenviron. Eng., 2021, 147(9): 04021093
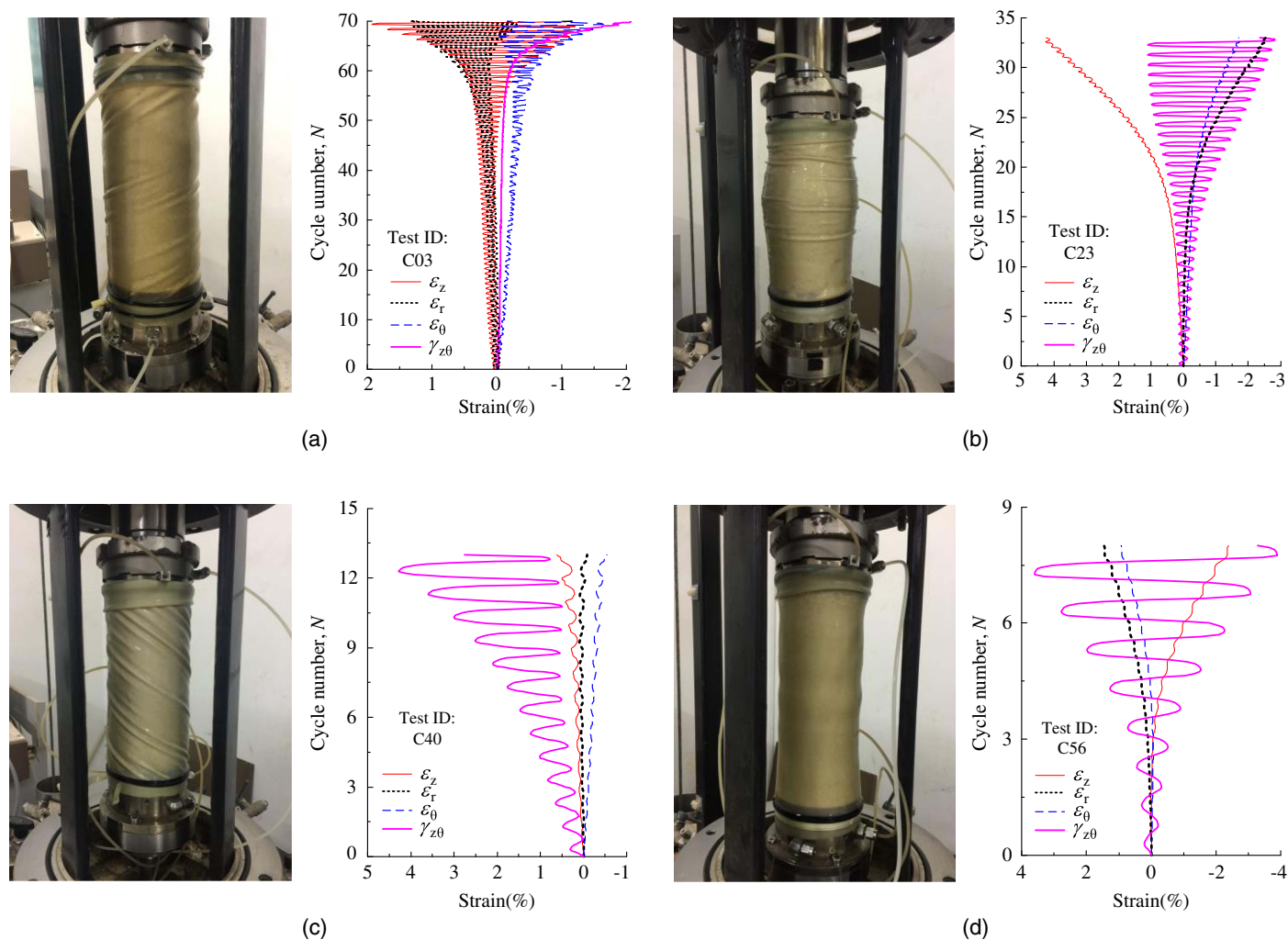
Fig. 11. Strain component responses of saturated coral sand specimens subjected to the 90° jump of principal stress at the same *CSR*: (a) isotropic consolidation; (b) anisotropic consolidation at $\alpha_0 = 0°$ and $k_c = 1.5$; (c) anisotropic consolidation at $\alpha_0 = 45°$ and $k_c = 1.5$; and (d) anisotropic consolidation at $\alpha_0 = 90°$ and $k_c = 1.5$.

isotropically consolidated case [Fig. 11(a)], various strain components obviously increase with the number of cycles N, and the values of ε_z and $\gamma_{z\theta}$ for larger N are slightly larger than those of ε_r and ε_θ. For the anisotropically consolidated cases [Figs. 11(b–d)], the features of the strain components are significantly affected by the consolidation paths, and the direction of ε_z is always opposite from the directions of ε_r and ε_θ. Fig. 12 exemplifies the typical undrained cyclic responses of isotropically and anisotropically consolidated saturated coral sand specimens subjected to the 90° jump or the continuous rotation of principal stress. As shown in Tables 5 and 6, the stability amplitudes of u_e locate in a range from 0.68 to $0.98p_0'$. For the anisotropically consolidated specimens, the effective q-p' stress paths for most of the specimens exhibit a trend of approaching $p' = 0$ as γ_{ga} reaches 2.5%, especially in tests with deviatoric stress reversals (e.g., C39, C49) [Fig. 12(c)]. This is regarded as an indicator that the tested specimen is about to fail. Note that p' does not reach zero for most anisotropically consolidated specimens, but irrecoverable plastic strain components accumulated in one side and the final values of u_e increase only slightly with N or almost reach a stable amplitude less than p_0' as γ_{ga} approaches 2.5%. The asymptotic stable amplitude of u_e significantly decreases as k_c increases [Fig. 12(a)], and it is strongly affected by the cyclic loading pattern [Fig. 12(b)]. This implies that the critical factor dominating

the onset of failure (or liquefaction) for anisotropically consolidated coral sand specimens is the generation of γ_{ga}.

For the isotropically consolidated undrained cyclic shear test, the occurrence of liquefaction is commonly defined as either the first transient $p' = 0$ state or the reach of a widely accepted strain level (Towhata and Ishihara 1985; Chen et al. 2020b). However, for the anisotropically consolidated undrained cyclic shear test, the failure criterion is always defined in terms of a certain level of axial strain (Chen et al. 2021b). It is found that initial liquefaction with near-zero effective stress state is observed as γ_{ga} reaches 2.5% for isotropically consolidated specimens. Based on the comprehensive experimental data, we found that the asymptotic stable amplitude of u_e is less than p_0' as γ_{ga} reaches 2.5%, and the progressive failure with accumulation of excessive strains develops over cycles for anisotropically consolidated specimens. Therefore, $\gamma_{ga} = 2.5\%$ can be used to mark the critical point after which the generalized shear strain increases dramatically.

Unified Formulation for Excess Pore Pressure Generation

Many methods have been proposed to quantitatively characterize the generation of u_e in saturated sandy soils subjected to cyclic loadings. Note that the generation of u_e with N of coral sand is quite different from that of Fujian sand for the 90° jump of principal

© ASCE 04021093-12 J. Geotech. Geoenviron. Eng.

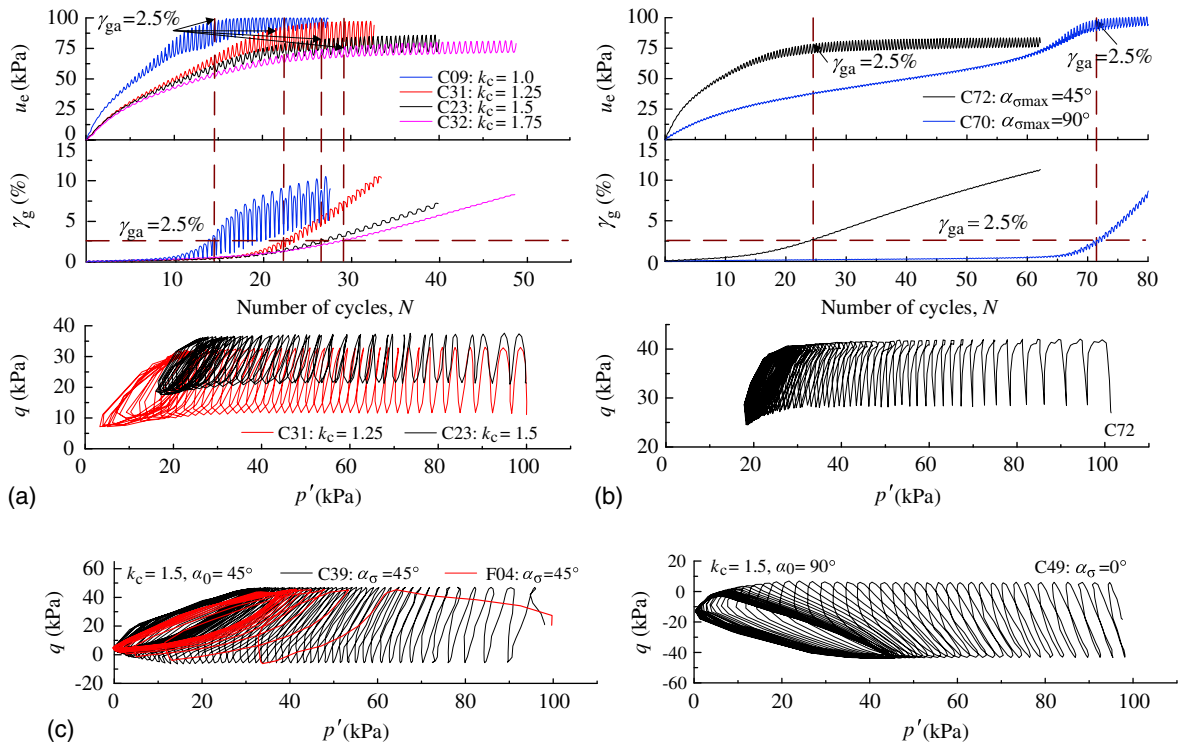J. Geotech. Geoenviron. Eng., 2021, 147(9): 04021093

Fig. 12. Typical undrained cyclic responses of isotropically and anisotropically consolidated saturated coral sand specimens: (a) varying k_c for Specimens C09, C23, C31, and C32; (b) varying $\alpha_{\sigma\max}$ for Specimens C70 and C72; and (c) deviatoric stress reversal Specimens C39 and C49.

stress tests, as shown in Fig. 6. Therefore, some limitations exist when these methods are applied to coral sand due to its high $CaCO_3$ content and unique fabric. By comparing Fig. 6 with Fig. 12, it is also noted that the generation patterns of u_e with N for coral sand specimens at various consolidation conditions and principal stress rotations are quite different even at the same CSR. Chen et al. (2020b) proposed a tangent function to describe the correlation between deviatoric strain amplitude γ_{qa} (in percent) and excess pore water pressure ratio r_u ($= u_e/p_0'$) for a nonplastic silt under isotropic consolidation and various cyclic loadings

$$\gamma_{qa} = A \tan\left(\frac{\pi}{2} r_u\right) \tag{1}$$

where $\gamma_{qa} = \varepsilon_1 - \varepsilon_3$; and $A =$ constant for the sandy soil in question. For most isotropically and anisotropically consolidated coral sand specimens, it is found that the values of radial strain ε_r ($=$ intermediate principal strain ε_2) may be as high as 2% or even higher, as exemplified in Fig. 11. Because the deviatoric strain γ_q does not include ε_2, it cannot account for the effect of ε_2 on r_u. However, the generalized shear strain γ_g includes the major, intermediate, and minor principal strains ε_1, ε_2, and ε_3, and hence can collectively account for the influence of all the strain components. In this regard, the generalized shear strain amplitude γ_{ga} is a more rational proxy to quantitatively describe the deformation. The simulation results for a liquefied, downhole array site in Japan (Chen et al. 2021a) also confirmed the advantage of using γ_{ga} to characterize the deformation associated with liquefaction.

For the undrained cyclic shear tests on coral sand specimens, the r_u is redefined in this study as follows:

$$r_u = u_e/u_{e2.5} \tag{2}$$

where $u_e =$ amplitude of excess pore water pressure at the Nth loading cycle; and $u_{e2.5} =$ stability amplitude of u_e at $\gamma_{ga} = 2.5\%$.

The values of $u_{e2.5}/p_0'$ for the tested coral sand specimens are given in Tables 5 and 6. Correspondingly, the number of cycles required to cause $\gamma_{ga} = 2.5\%$ is denoted by N_f.

Fig. 13 plots γ_{ga} against r_u for the coral sand specimens subjected to the 90° jump or the continuous rotation of principal stress. A striking feature of the plots is that data for isotropic consolidation tests or each group of anisotropic consolidation tests with the same α_0 and k_c fall in a quite narrow range, suggesting that a unified form of the relationships exists between γ_{ga} and r_u regardless of the cyclic loading patterns and the initial static shear stress levels. Thus, a unified formulation between γ_{ga} and r_u for coral sand specimens is proposed as

$$\gamma_{ga} = A \tan\left(B \times \frac{\pi}{2} r_u\right) \tag{3}$$

where A and $B =$ best-fitting coefficients. The R-square values of a nonlinear regression using Eq. (3) to fit the data in Figs. 13(a–d) are in the range of 0.91–0.93. In addition, Fig. 13(e) plots all the experimental data together for isotropically and anisotropically consolidated specimens, and the best-fitting coefficients A and B are 0.414 and 0.899, respectively, with an R-square value of 0.89. The significant implication is that the unified formulation of Eq. (3) is valid for all the consolidation conditions and cyclic loadings considered, although the coefficients A and B are considered to be material-specific constants. Thus, a unified formulation for predicting the r_u as a function of γ_{ga} can be rewritten as follows:

$$r_u = \frac{2}{\pi}\frac{1}{B}\arctan\left(\frac{\gamma_{ga}}{A}\right) \tag{4}$$

In addition, we found in Fig. 13 that $\gamma_{ga} = 2.5\%$ can be approximately considered as the critical point after which γ_{ga} increases
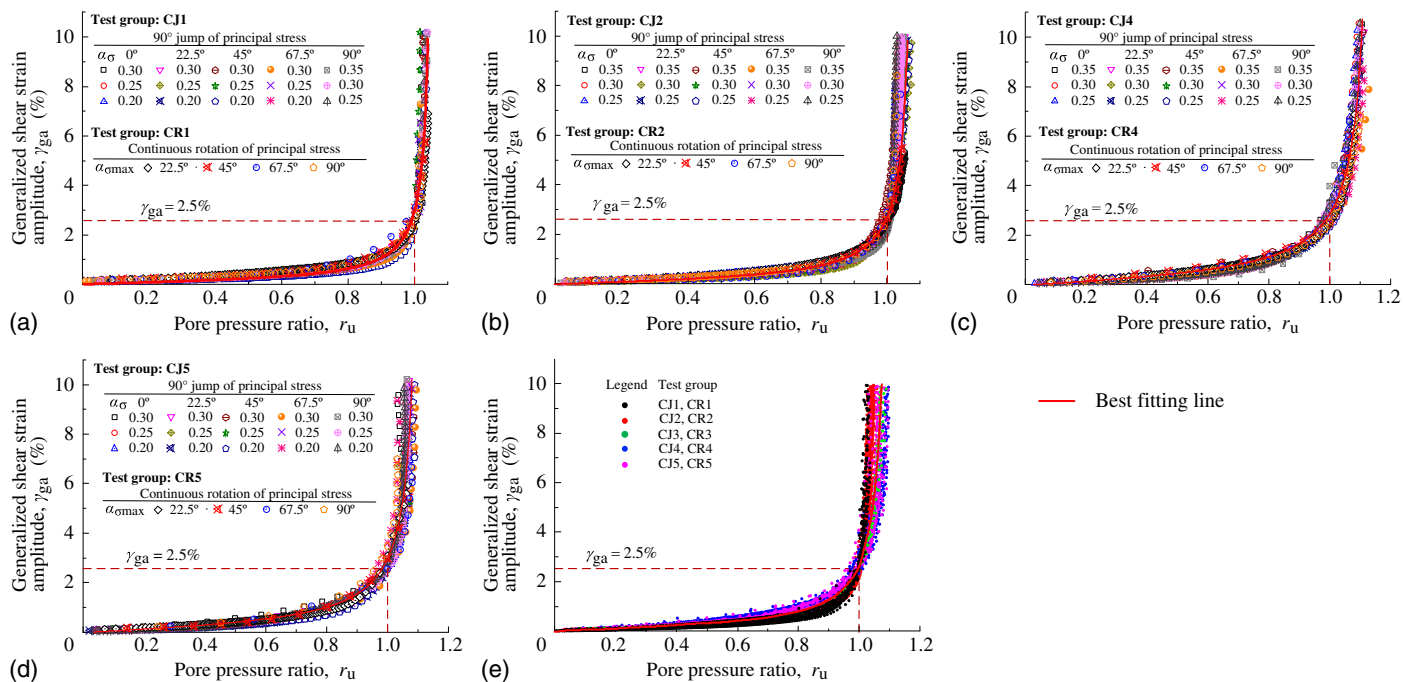
© ASCE 04021093-13 J. Geotech. Geoenviron. Eng.

J. Geotech. Geoenviron. Eng., 2021, 147(9): 04021093

Fig. 13. Correlation between γ_{ga} and r_u of saturated coral sand specimens subjected to various patterns of principal stress rotation: (a) isotropic consolidation; (b) anisotropic consolidation at $\alpha_0 = 0°$ and $k_c = 1.5$; (c) anisotropic consolidation at $\alpha_0 = 45°$ and $k_c = 1.5$; (d) anisotropic consolidation at $\alpha_0 = 90°$ and $k_c = 1.5$; and (e) all tests.
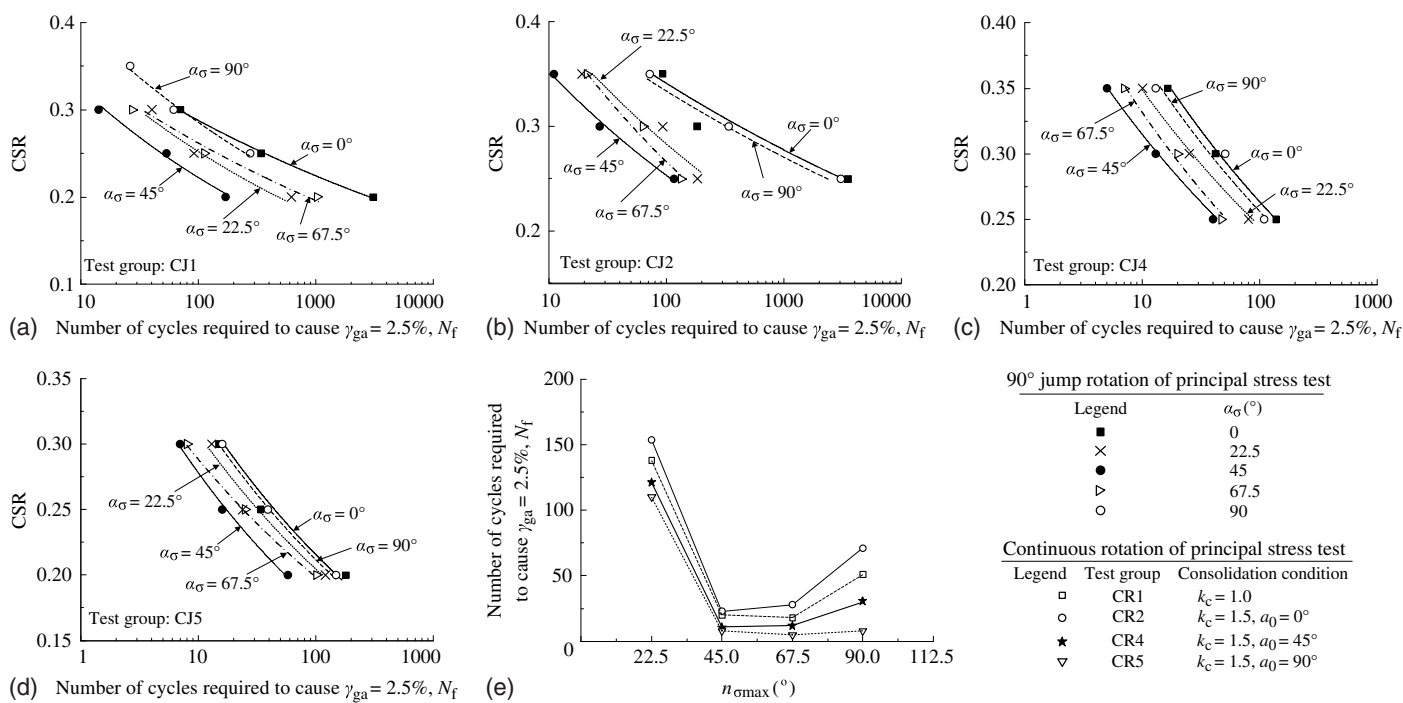

Fig. 14. Correlation between CSR and N_f of saturated coral sand specimens subjected to the 90° jump of principal stress: (a) isotropic consolidation; (b) anisotropic consolidation at $\alpha_0 = 0°$ and $k_c = 1.5$; (c) anisotropic consolidation at $\alpha_0 = 45°$ and $k_c = 1.5$; (d) anisotropic consolidation at $\alpha_0 = 90°$ and $k_c = 1.5$; and (e) correlation between $\alpha_{\sigma max}$ and N_f under continuous rotation of principal stress.

dramatically up to 10% or even more. It implies that it is appropriated to adopt $\gamma_{ga} = 2.5\%$ as the consistent criterion of liquefaction (or failure) for both isotropically and anisotropically consolidated coral sand specimens.

Unified Formulation for Undrained Cyclic Resistance

Fig. 14 shows the correlation between CSR and N_f for the tested coral sand specimens. Clearly, the CSR required to trigger liquefaction is highly affected by the consolidation conditions and cyclic

© ASCE   04021093-14   J. Geotech. Geoenviron. Eng.

J. Geotech. Geoenviron. Eng., 2021, 147(9): 04021093

stress paths. For the 90° jump of principal stress tests, the CSR versus N_f curves at $\alpha_\sigma = 45°$ and $\alpha_\sigma = 0°$ are located at the bottom and top of the graphs [Figs. 14(a–d)], respectively. It implies that the saturated coral sand specimens under the cyclic stress path of $\alpha_\sigma = 45°$ are most susceptible to liquefaction for the same consolidation condition. This result is consistent with the test result on Nantong silt (Chen et al. 2020b). For the continuous rotation of principal stress tests, the N_f versus $\alpha_{\sigma max}$ curves along the inclination of $\alpha_0 = 90°$ and 0° at fixed $k_c = 1.5$ are located at the bottom and top of the graph [Fig. 14(e)], respectively. Meanwhile, N_f at $\alpha_{\sigma max}$ ranging from 45° to 67.5° was almost the lowest under the same consolidation condition. This implies that, for consolidation condition $\alpha_0 = 90°$ and $k_c = 1.5$, the cases of $\alpha_{\sigma max} = 45°–67.5°$ are most susceptible to liquefaction. Similarly, for isotropically consolidated cases, the saturated Fraser River sand at $\alpha_{\sigma max} = 45°$ (Sivathayalan et al. 2015) is most susceptible to liquefaction.

Chen et al. (2020b) proposed a new proxy, termed the unit cyclic stress ratio (USR), to quantitatively describe the liquefaction resistance of sandy soils, and a unique correlation between USR and N_f under isotropic consolidation was established as follows (Chen et al. 2020b):

$$USR = C_1 C_2 CSR \qquad (5)$$

where parameters C_1 and C_2 are defined as follows:

$$C_1 = A_{p0}/A_M \qquad (6)$$

$$C_2 = (1 - A_{q0}/A_{p0})^{C_3} \qquad (7)$$

$$A_{p0} = \int_0^T \sqrt{\left(\frac{W(t)}{\pi(r_o^2 - r_i^2)}\right)^2 / 4 + \left(\frac{3M_T(t)}{2\pi(r_o^3 - r_i^3)}\right)^2}\, dt \qquad (8)$$

$$A_{q0} = \left| \int_0^T (\sigma_z(t) - p)dt \right| = \left| \int_0^T \left(\frac{W(t)}{\pi(r_o^2 - r_i^2)}\right) dt \right| \qquad (9)$$

where A_M = reference value and $A_M = 1.27 q_{am} T$; T = cyclic loading period; C_3 = parameter possibly reflecting the effect of soil property; and 0.1 = appropriate value for C_3.

Fig. 15 plots USR against N_f for the isotropically and anisotropically consolidated coral sand specimens. The data for each group fall within a narrow band and can be fitted well by a trend line. It implies that the parameters C_1 and C_2 in the USR expression can significantly reduce the influence of cyclic loading patterns and paths on the liquefaction resistance curve. This observation is

consistent with the finding of Chen et al. (2020b) obtained from tests on Nantong silt. However, as shown in Fig. 15(b), the data for three different consolidation paths are distinctly separated and cannot collapse to the same narrow band. In addition, it is noted that the USR versus N_f curve of the coral sand is positioned much higher than those of Fujian sand and Fraser River sand (Sivathayalan et al. 2015), meaning that the coral sand has a much higher liquefaction resistance than the siliceous sands.

To better understand and compare liquefaction susceptibility of saturated coral sand under various consolidation conditions and cyclic loadings, an attempt was made here to quantify the liquefaction resistance by the generalized unit cyclic stress ratio USR_g instead of USR. Based on the twin shear strength theory proposed by Yu (2004), the maximum principal shear stress τ_{13} and the maximum principal normal stress σ_{13} are introduced here first to define USR_g

$$\sigma_{13} = (\sigma_1 + \sigma_3)/2 \qquad (10)$$

$$\tau_{13} = (\sigma_1 - \sigma_3)/2 \qquad (11)$$

Thus, the maximum principal shear stress τ_{13c} and the effective maximum principal normal stress σ'_{13c} after consolidation can be expressed as

$$\sigma'_{13c} = (\sigma'_{1c} + \sigma'_{3c})/2 = (\sigma'_{zc} + \sigma'_{\theta c})/2 \qquad (12)$$

$$\tau_{13c} = (\sigma'_{1c} - \sigma'_{3c})/2 = \sqrt{(\sigma'_{zc} - \sigma'_{\theta c})^2/4 + \tau_{z\theta c}^2} \qquad (13)$$

Note that σ'_{2c} is perpendicular to the consolidation stress plane determined by $(\sigma_z - \sigma_\theta)/2$ and $\tau_{z\theta}$ and its influence can be ignored for simplicity. Then, under the assumption that σ'_2 and p'_{ic} are equal to p'_{oc}, σ'_{13c}, and τ_{13c} can be expressed by the following forms:

$$\sigma'_{13c0} = \frac{\sigma'_{zc0} + p'_{oc}}{2} = \frac{1}{2}\frac{W_c}{\pi(r_o^2 - r_i^2)} + p'_{oc} \qquad (14)$$

$$\tau_{13c0} = \sqrt{\frac{1}{4}(\sigma_{zc0} - p'_{oc})^2 + \tau_{z\theta c}^2}$$

$$= \sqrt{\frac{1}{4}\left(\frac{W_c}{\pi(r_o^2 - r_i^2)}\right)^2 + \left(\frac{3M_{Tc}}{2\pi(r_o^3 - r_i^3)}\right)^2} \qquad (15)$$

For some continuous rotation of principal stress paths, the waveform function of cyclic loading $W(t)$ is unsymmetrical, which can
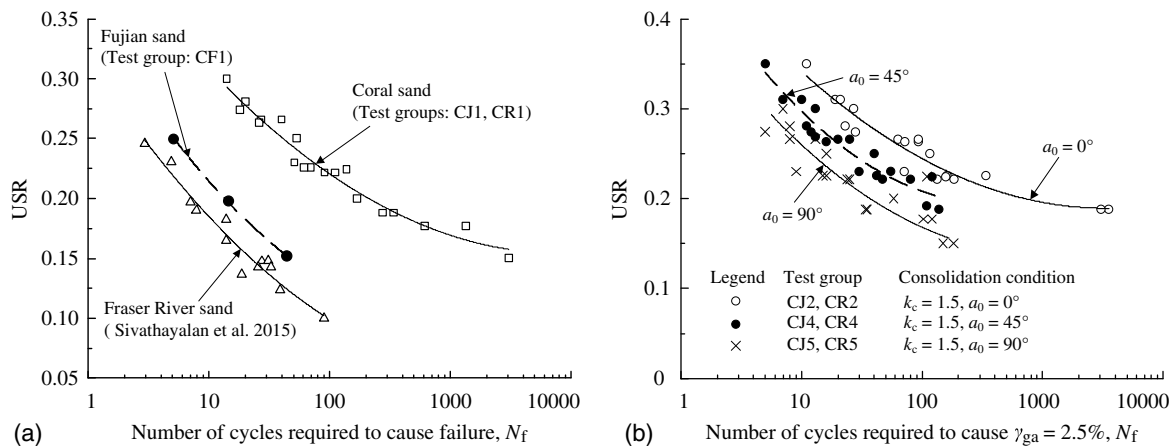

Fig. 15. USR versus N_f under various consolidation conditions and cyclic loading patterns: (a) isotropic consolidation; and (b) anisotropic consolidation.

enhance or weaken the effect of consolidation, especially the path-dependent anisotropic consolidations. To quantify the influence of $W(t)$ under anisotropic consolidations, the mean value of $W(t)$, termed W_{cyc}, is adopted here instead of the peak value. W_{cyc} can be expressed as follows:

$$W_{cyc} = \frac{1}{T} \int_0^T W(t)dt \tag{16}$$

Note that W_{cyc} enhances (or weakens) the effect of consolidation if the value of W_{cyc} is positive (or negative). For simplicity, by defining $W_e = W_c + \sqrt{k_c - 1}W_{cyc}$, σ'_{13c0} and τ_{13c0} in Eqs. (14) and (15) can be rewritten as follows:

$$\sigma'_{13e} = \frac{1}{2}\frac{W_e}{\pi(r_o^2 - r_i^2)} + p'_{oc} \tag{17}$$

$$\tau_{13e} = \sqrt{\frac{1}{4}\left[\frac{W_e}{\pi(r_o^2 - r_i^2)}\right]^2 + \left[\frac{3M_{Tc}}{2\pi(r_o^3 - r_i^3)}\right]^2} \tag{18}$$

Now, a new proxy USR_g representing the liquefaction resistance in universal correlation for various consolidation conditions and cyclic loadings is proposed as follows:

$$USR_g = \frac{USR}{D_1 D_2} = \frac{C_1 C_2}{D_1 D_2}CSR \tag{19}$$

where parameters D_1 and D_2 are defined as follows:

$$D_1 = (\sigma'_{13e}/p'_{oc})^{D_3} \tag{20}$$

$$D_2 = \sqrt{1 - (\tau_{13e}/\sigma'_{13e})^2} \tag{21}$$

where D_3 = a parameter considering the ambiguous effect of anisotropic consolidations. In the interpretation of both the test data and the data in literature, the value of D_3 is approximately 1.0 for common anisotropic consolidation, 1.2 for K_0 consolidation, and 1.6 for constant normal stress consolidation [i.e., initial effective normal stress on the 45° plane = constant $(\sigma'_{1c} + \sigma'_{3c})/2$]. The values of D_1 and D_2 for each test are given in Tables 5 and 6.

For isotropic consolidations, $USR_g = USR$ because $W_c = W_{cyc} = M_{Tc} = 0$, and thus $D_1 = D_2 = 1$. Fig. 16 plots USR_g versus N_f for all the specimens under the various consolidation and cyclic loading conditions. An important finding from Fig. 16 is that all the data fall into a very narrow band and a unique form of the correlations exists between USR_g and N_f. It is evident that the parameters D_1 and D_2 in the USR_g expression can virtually eliminate the influence of consolidation conditions on the liquefaction resistance.

Validation of the Universal Formulation Applicability and Discussion

To further validate the applicability of the proxy USR_g, relevant data in the literature have been compiled and analyzed, as shown in Fig. 17. The data of Zhou et al. (2019, 2020) were from UCTS tests on South China Sea coral sand subjected to the 90° jump of principal stress ($D_{rc} = 33\%-37\%$; failure criterion: single amplitude shear strain $\gamma_{sa} = 2.5\%$ for isotropic consolidation and cumulative shear strain $\gamma_{cu} = 5\%$ for the anisotropic consolidation at $\alpha_\sigma = 45°$; $\gamma_{ga} = 5\%$ for the cases of isotropic and anisotropic consolidations at $\alpha_\sigma = 0°$ and 22.5°). The data of Rasouli et al. (2020) were from K_0-consolidated UCSS tests on Hormuz Island coral sand ($D_{rc} = 31.7\%-36\%$; $K_0 = 0.22$; failure criterion: double amplitude shear strain $\gamma_{da} = 6\%$ or $\gamma_{cu} = 5\%$). The data of Flora et al. (2012) were from isotropically consolidated and K_0-consolidated undrained cyclic triaxial tests on sandy gravel (failure criterion: $r_u = 0.9$ for isotropically consolidated specimens; double amplitude axial strain $\varepsilon_{da} = 2.5\%$ for K_0 − consolidation specimens). The data of Yang and Sze (2011a) were from constant normal stress consolidated undrained cyclic triaxial tests on Toyoura clean sand, and the data of Wei and Yang (2019) were for Toyoura sand with 10% fines content ($D_{rc} = 20\%$; failure criterion: $\varepsilon_{da} = 5\%$ for cyclic mobility failure, or peak axial strain $\varepsilon_{pa} = 5\%$ for plastic strain accumulation failure). It is consistently observed that each data set falls into a narrow band, and the prediction using the proposed relationship for USR_g and N_f, Eq. (19), fits the experimental data well. Considering the variability of test materials and test methods in these studies, it can be concluded that a universal and unique correlation between USR_g and N_f exists for various sandy soils, irrespective of consolidation conditions, cyclic loading patterns, and failure criteria.

For conventional isotropically and anisotropically consolidated undrained cyclic triaxial tests, the cyclic shear effect plane with the maximum ratio of cyclic shear stress amplitude to normal consolidation stress was defined as the maximum cyclic shear effect plane (weakest plane) of a specimen (Zhang 1984; Chen et al. 2021b). Then, a universal form of cyclic stress ratio on the maximum cyclic shear effect plane (CSR_α) was derived

$$CSR_\alpha = \sigma_d/(2\sigma'_{3c}\sqrt{k_c}) = CSR/\sqrt{k_c} \tag{22}$$

where σ_d = applied stress amplitude of sinusoidal cyclic axial loading. For isotropically consolidation conditions, $k_c = 1$, and therefore $CSR_\alpha = CSR$. For conventional undrained cyclic triaxial tests, which only involve sinusoidal cyclic axial loading $W(t)$ [i.e., $M_T(t) = p_o(t) = p_i(t) = 0$], inner radius $r_i = 0$, then $\sigma'_{1c} = \sigma'_{zc}$, $\sigma'_{3c} = \sigma'_{\theta c} = p'_{oc}$, $\tau_{z\theta c} = 0$, $W_{cyc} = 0$, $A_{q0} = 0$, and $A_{p0} = A_M$. Therefore, two correlations can be derived: $\sigma'_{13e} = (\sigma'_{1c} + \sigma'_{3c})/2$ and $\tau_{13e} = (\sigma'_{1c} - \sigma'_{3c})/2$. Then, one can establish that $C_1 = C_2 = 1$, $D_1 = (k_c + 1)/2$, and $D_2 = 2\sqrt{k_c}/(k_c + 1)$, leading to $D_1 D_2 = \sqrt{k_c}$ and $USR_g = CSR_\alpha$.

In summary, the new proxy USR_g is more physically rational and has much wider applicability than the conventional CSR. Further validations of this new proxy using measured data on various sandy soils under various patterns of consolidation condition and cyclic loading couplings would be worthwhile.
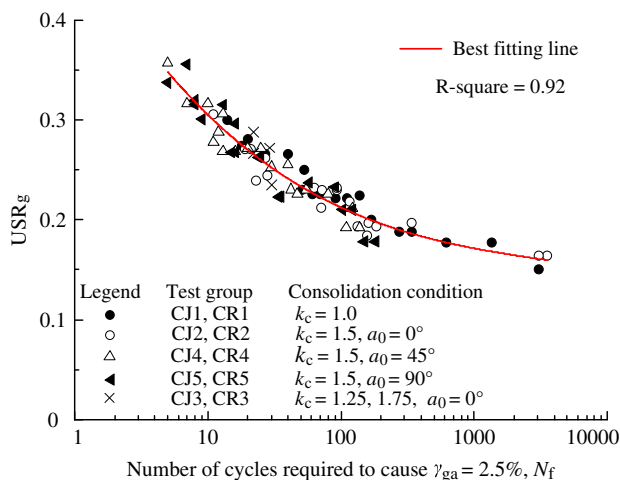

Fig. 16. Correlation between USR_g and N_f based on all test data.

Legend	Test group	Consolidation condition
●	CJ1, CR1	$k_c = 1.0$
○	CJ2, CR2	$k_c = 1.5$, $a_0 = 0°$
△	CJ4, CR4	$k_c = 1.5$, $a_0 = 45°$
◀	CJ5, CR5	$k_c = 1.5$, $a_0 = 90°$
×	CJ3, CR3	$k_c = 1.25, 1.75$, $a_0 = 0°$

© ASCE   04021093-16   J. Geotech. Geoenviron. Eng.

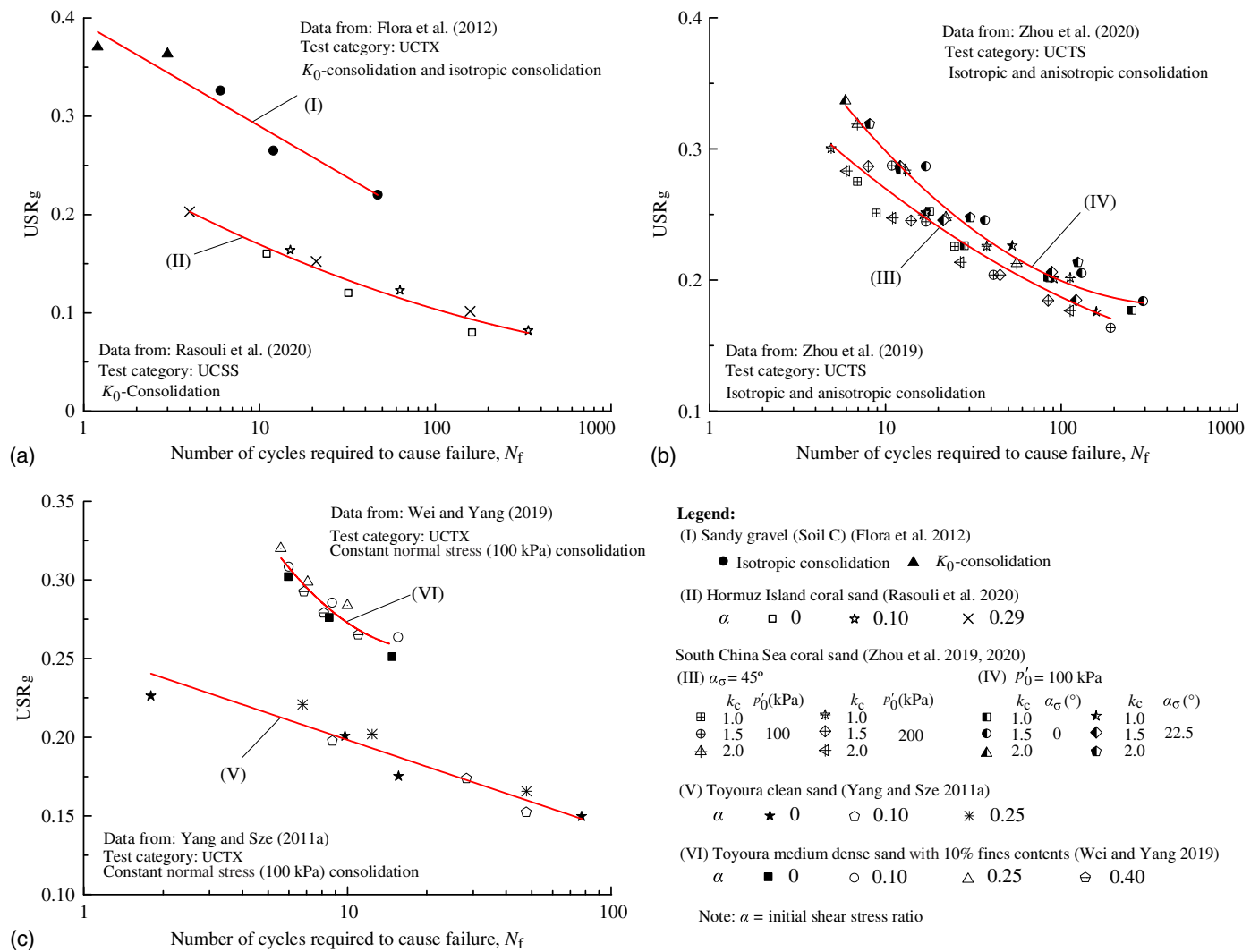J. Geotech. Geoenviron. Eng., 2021, 147(9): 04021093

Fig. 17. Validation of the USR_g formulation [Eq. (19)] using literature data: (a) Hormuz Island coral sand (data from Rasouli et al. 2020) and sandy gravel (Soil C) (data from Flora et al. 2012); (b) South China Sea coral sand (data from Zhou et al. 2019, 2020); and (c) Toyoura clean sand (data from Yang and Sze 2011a) and Toyoura sand with 10% fine contents (data from Wei and Yang 2019).

Conclusions

This paper presents interesting results from undrained monotonic and cyclic shear tests on a coral sand conducted using a hollow cylinder torsional shear apparatus. Focus was placed on the lique-faction susceptibility under different patterns of principal stress rotation and different consolidation conditions. The main conclusions can be summarized as follows:

1. The dilative response in undrained monotonic shearing is an inherent behavior of the coral sand. The stress-induced anisotropy relates closely to both consolidation and monotonic shearing paths and is significant on the shear resistance parameters S_{PT} and ϕ'_{PT} at the phase transformation state. The S_{PT} along the 45° stress path is lowest under the isotropic consolidation, while the S_{PT} along the inclination of the initial major principal stress is largest under the anisotropic consolidations.

2. The generation of excess pore water pressure, u_e, is significantly affected by the coupling patterns of consolidation conditions and cyclic loadings. For all tested conditions, a virtually unique relationship was established between the generalized shear strain amplitude, γ_{ga}, and the pore water pressure ratio, r_u. The strain level of $\gamma_{ga} = 2.5\%$ represents a threshold state at

which the first transient near-zero effective stress state occurs or the amplitude of u_e is stable, and it can be taken as a proper failure criterion. Moreover, the generation rate of u_e in the tested coral sand is much lower than that of the tested siliceous sand.

3. In the cases of 90° jump of principal stress, the coral sand is most susceptible to liquefaction at $\alpha_\sigma = 45°$ stress path, irrespective of consolidation conditions. In the cases of continuous rotation of principal stress, the coral sand under the anisotropic consolidations along the bedding plane is most susceptible to liquefaction, whereas at a specific anisotropic consolidation path, the cases of $\alpha_{\sigma max}$ varying from 45° to 67.5° are most critical.

4. The new liquefaction resistance proxy, termed as generalized unit cyclic stress ratio (USR_g), can properly eliminate the coupled effects of consolidation conditions and cyclic loading patterns on the liquefaction resistance. A virtually unique relationship exists between USR_g and the number of cycles N_f required to cause $\gamma_{ga} = 2.5\%$ for all testing conditions. This relationship is validated using independent test data in the literature, indicating a wide applicability. Further validation using test data on different sandy soils under various consolidation conditions and cyclic loading patterns is worthwhile.

Data Availability Statement

All data, models, and code generated or used during the study appear in the published article.

Acknowledgments

References

ASTM. 2011. *Standard practice for classification of soils for engineering purposes (Unified Soil Classification System)*. ASTM D2487. West Conshohocken, PA: ASTM.

ASTM. 2013. *Standard test method for load controlled cyclic triaxial strength of soil*. ASTM D5311/D5311M. West Conshohocken, PA: ASTM.

Boulanger, R. W. 2003. "Relating K_α to relative state parameter index." *J. Geotech. Geoenviron. Eng.* 129 (8): 770–773. https://doi.org/10.1061/(ASCE)1090-0241(2003)129:8(770).

Brandes, H. G. 2011. "Simple shear behavior of calcareous and quartz sands." *Geotech. Geol. Eng.* 29 (1): 113–126. https://doi.org/10.1007/s10706-010-9357-x.

Burke, L., K. Reytar, M. Spalding, and A. Perry. 2011. *Reefs at risk revisited*. Washington, DC: World Resources Institute.

Chen, G. X., Y. Z. Wang, D. F. Zhao, K. Zhao, and J. Yang. 2021a. "A new effective stress method for nonlinear site response analyses." *Earthquake Eng. Struct. Dyn.* 50: 1595–1611. https://doi.org/10.1002/eqe.3414.

Chen, G. X., Q. Wu, T. Sun, K. Zhao, E. Q. Zhou, L. Y. Xu, and Y. G. Zhou. 2021b. "Cyclic behaviors of saturated sand-gravel mixtures under undrained cyclic triaxial loading." *J. Earthquake Eng.* 25 (4): 756–789. https://doi.org/10.1080/13632469.2018.1540370.

Chen, G. X., Q. Wu, K. Zhao, Z. F. Shen, and J. Yang. 2020a. "A binary packing material-based procedure for evaluating soil liquefaction triggering during earthquakes." *J. Geotech. Geoenviron. Eng.* 146 (6): 04020040. https://doi.org/10.1061/(ASCE)GT.1943-5606.0002263.

Chen, G. X., Q. Wu, Z. L. Zhou, W. J. Ma, W. Y. Chen, K. Sara, and J. Yang. 2020b. "Undrained anisotropy and cyclic resistance of saturated silt subjected to various patterns of principal stress rotation." *Géotechnique* 70 (4): 317–331. https://doi.org/10.1680/jgeot.18.P.180.

Chock, G., et al. 2006. *Compilation of observations of the October 15, 2006 Kiholo Bay (Mw 6.7) and Mahukona (Mw 6.0) Earthquakes, Hawai'i*. Rep. No. 31. Oakland, CA: Earthquake Engineering Research Institute.

Flora, A., S. Lirer, and F. Silvestri. 2012. "Undrained cyclic resistance of undisturbed gravelly soils." *Soil Dyn. Earthquake Eng.* 43 (Dec): 366–379. https://doi.org/10.1016/j.soildyn.2012.08.003.

Georgiannou, V. N., M. Konstadinou, and P. Triantafyllos. 2018. "Sand behavior under stress states involving principal stress rotation." *J. Geotech. Geoenviron. Eng.* 144 (6): 04018028. https://doi.org/10.1061/(ASCE)GT.1943-5606.0001878.

Giretti, D., V. Fioravante, K. Been, and S. Dickenson. 2018. "Mechanical properties of a carbonate sand from a dredged hydraulic fill." *Géotechnique* 68 (5): 410–420. https://doi.org/10.1680/jgeot.16.P.304.

Harder, L. F., Jr., and R. W. Boulanger. 1997. "Application of K_σ and K_α correction factors." In *Proc., of the NCEER Workshop on Evaluation of Liquefaction Resistance of Soils*, 167–190. Buffalo, NY: National Center for Earthquake Engineering Research, State University of New York.

Hight, D. W., A. Gens, and M. J. Symes. 1983. "The development of a new hollow cylinder apparatus for investigating the effects of principal stress rotation in soils." *Géotechnique* 33 (4): 355–383. https://doi.org/10.1680/geot.1983.33.4.355.

Hyodo, M., A. F. L. Hyde, and N. Aramaki. 1998. "Liquefaction of crushable soils." *Géotechnique* 48 (4): 527–543. https://doi.org/10.1680/geot.1998.48.4.527.

Mao, X., and M. Fahey. 2003. "Behaviour of calcareous soils in undrained cyclic simple shear." *Géotechnique* 53 (8): 715–727. https://doi.org/10.1680/geot.2003.53.8.715.

Morioka, B. T., and P. G. Nicholson. 2000. "Evaluation of the liquefaction potential of calcareous sand." In Vol. II of *Proc., 10th Int. Offshore and Polar Engineering Conf.*, 494–500. Mountain View, CA: International Society of Offshore and Polar Engineers.

Nakata, Y., M. Hyodo, H. Murata, and N. Yasufuku. 1998. "Flow deformation of sands subjected to principal stress rotation." *Soils Found.* 38 (2): 115–128. https://doi.org/10.3208/sandf.38.2_115.

Oda, M., S. Nemat-Nasser, and J. Konishi. 1985. "Stress-induced anisotropy in granular masses." *Soils Found.* 25 (3): 85–97. https://doi.org/10.3208/sandf1972.25.3_85.

Olson, S. M., R. A. Green, S. Lasley, N. Martin, B. R. Cox, E. Rathje, J. Bachhuber, and J. French. 2011. "Documenting liquefaction and lateral spreading triggered by the 12 January 2010 Haiti earthquake." Supplement, *Earthquake Spectra* 27 (S1): 93–116. https://doi.org/10.1193/1.3639270.

Rasouli, M. R., M. Moradi, and A. Ghalandarzadeh. 2020. "Effects of initial static shear stress orientation on cyclic behavior of calcareous sand." *Mar. Georesour. Geotechnol.* 39 (5): 554–568. https://doi.org/10.1080/1064119X.2020.1726535.

Salem, M., H. Elmamlouk, and S. Agaiby. 2013. "Static and cyclic behavior of North Coast calcareous sand in Egypt." *Soil Dyn. Earthquake Eng.* 55 (Dec): 83–91. https://doi.org/10.1016/j.soildyn.2013.09.001.

Sandoval, E. A., and M. A. Pando. 2012. "Experimental assessment of the liquefaction resistance of calcareous biogenous sands." *Earth Sci. Res. J.* 16 (1): 55–63.

Sharma, S. S., and M. A. Ismail. 2006. "Monotonic and cyclic behavior of two calcareous soils of different origins." *J. Geotech. Geoenviron. Eng.* 132 (12): 1581–1591. https://doi.org/10.1061/(ASCE)1090-0241(2006)132:12(1581).

Shedlock, K. M., D. Giardini, G. Grünthal, and P. Zhang. 2000. "The GSHAP global seismic hazard map." *Seismol. Res. Lett.* 71 (6): 679–686. https://doi.org/10.1785/gssrl.71.6.679.

Sivathayalan, S., P. Logeswaran, and V. Manmatharajan. 2015. "Cyclic resistance of a loose sand subjected to rotation of principal stresses." *J. Geotech. Geoenviron. Eng.* 141 (3): 04014113. https://doi.org/10.1061/(ASCE)GT.1943-5606.0001250.

Sivathayalan, S., and Y. P. Vaid. 2002. "Influence of generalized initial state and principal stress rotation on the undrained response of sands." *Can. Geotech. J.* 39 (1): 63–76. https://doi.org/10.1139/t01-078.

Sze, H. Y., and J. Yang. 2014. "Failure modes of sand in undrained cyclic loading: Impact of sample preparation." *J. Geotech. Geoenviron. Eng.* 140 (1): 152–169. https://doi.org/10.1061/(ASCE)GT.1943-5606.0000971.

Towhata, I., and K. Ishihara. 1985. "Undrained strength of sand undergoing cyclic rotation of principal stress axes." *Soils Found.* 25 (2): 135–147. https://doi.org/10.3208/sandf1972.25.2_135.

Vahdani, S., R. Pyke, and U. Siriprusanen. 1994. "Liquefaction of calcareous sands and lateral spreading experienced in Guam as a result of the 1993 Guam earthquake." In *Proc., 5th US-Japan Workshop on Earthquake Resistant Design of Lifeline Facilities and Countermeasures against Soil Liquefaction*, 117–134. Buffalo, NY: National Center for Earthquake Engineering Research.

Wei, X., and J. Yang. 2019. "Cyclic behavior and liquefaction resistance of silty sands with presence of initial static shear stress." *Soil Dyn. Earthquake Eng.* 122 (Jul): 274–289. https://doi.org/10.1016/j.soildyn.2018.11.029.

Yang, J., and H. Y. Sze. 2011a. "Cyclic behaviour and resistance of saturated sand under nonsymmetrical loading conditions." *Géotechnique* 61 (1): 59–73. https://doi.org/10.1680/geot.9.P.019.

© ASCE   04021093-18   J. Geotech. Geoenviron. Eng.

J. Geotech. Geoenviron. Eng., 2021, 147(9): 04021093

Yang, J., and H. Y. Sze. 2011b. "Cyclic strength of sand under sustained shear stress." *J. Geotech. Geoenviron. Eng.* 137 (12): 1275–1285. https://doi.org/10.1061/(ASCE)GT.1943-5606.0000541.

Yu, M. H. 2004. *Unified strength theory and its applications*. Berlin: Springer.

Zhang, K. X. 1984. "Stress condition inducing liquefaction of saturated sand." [In Chinese.] *Earthquake Eng. Eng. Vibr.* 4 (1): 99–109. https://doi.org/10.13197/j.eeev.1984.01.009.

Zhou, X. Z., Y. M. Chen, W. W. Li, and H. L. Liu. 2019. "Monotonic and cyclic behaviors of loose anisotropically consolidated calcareous sand in torsional shear tests." *Mar. Georesour. Geotechnol.* 37 (4): 438–451. https://doi.org/10.1080/1064119X.2018.1449274.

Zhou, X. Z., Y. M. Chen, H. L. Liu, and X. L. Zhang. 2020. "Experimental study on the cyclic behavior of loose calcareous sand under linear stress paths." *Mar. Georesour. Geotechnol.* 38 (3): 277–290. https://doi.org/10.1080/1064119X.2019.1567631.

© ASCE   04021093-19   J. Geotech. Geoenviron. Eng.

J. Geotech. Geoenviron. Eng., 2021, 147(9): 04021093